ORNL/TM-8648
Dist. Category UC-20

Contract No. W-7405-eng-26

ORNL/TM--8648

DE83 012340

FUSION ENERGY DIVISION

MHD ACTIVITY IN THE ISX-B TOKAMAK: EXPERIMENTAL RESULTS AND THEORETICAL INTERPRETATION

B. A. Carreras, J. L. Dunlap, W. A. Cooper, R. A. Dory, T. C. Hender,
M. Murakami, V. K. Paré, A. J. Wootton
Fusion Energy Division

J. D. Bell, L. A. Charlton, H. R. Hicks, J. A. Holmes
V. E. Lynch, R. M. Wieland
Computer Sciences

P. H. Diamond and P. L. Similon
Institute for Fusion Studies
University of Texas
Austin, Texas 78712

Date Published - June 1983

Prepared by the
OAK RIDGE NATIONAL LABORATORY
Oak Ridge, Tennessee 37830
operated by
UNION CARBIDE CORPORATION
for the
U.S. DEPARTMENT OF ENERGY

CONTENTS

ABSTRACT

The observed spectrum of magnetohydrodynamic (MHD) fluctuations in the Impurity Study Experiment (ISX-B) tokamak is clearly dominated by the $n = 1$ mode when the $q = 1$ surface is in the plasma. This fact agrees well with theoretical predictions based on three-dimensional (3-D) resistive MHD calculations. They show that the $(m = 1;\ n = 1)$ mode is the dominant instability. It drives other $n = 1$ modes through toroidal coupling and $n > 1$ modes through nonlinear couplings. These theoretically predicted mode structures have been compared in detail with the experimentally measured wave forms (using arrays of soft x-ray detectors). The agreement is excellent. More detailed comparisons between theory and experiment have required careful reconstructions of the ISX-B equilibria. The equilibria so constructed have permitted a precise evaluation of the ideal MHD stability properties of ISX-B. The present results indicate that the high-beta ISX-B equilibria are marginally stable to finite-n ideal MHD modes. The resistive MHD calculations also show that at finite beta there are unstable resistive pressure-driven modes. For low-β_p equilibria these modes saturate at very low level and their evolution has little effect on the dominant $(m = 1;\ n = 1)$ mode. However, with increasing β_p they become more important. Their n spectrum is concentrated at low mode number and is broad. Analytic calculations indicate that their saturated kinetic energy scales like $(\varepsilon\beta_p)^{5/3}\eta^{4/3}$. These scalings have been confirmed by numerical results. The resistive ballooning modes are good candidates for the explanation of the confinement detericration at high β_p in ISX-B. The transport effects induced by them are estimated from the theory and are found to be mainly thermal electron conduction losses. An expression for χ_e is derived, and it yields values that agree well with those from the experiment.

I. INTRODUCTION

Through the Impurity Study Experiment (ISX-B) tokamak with up to 3 MW of beam heating power, about ten times its ohmic heating power, a totally new regime of tokamak plasmas is being explored. The results obtained [1-4] raise many questions related to the stability of such plasmas. These questions can be separated into three areas: (1) ideal magnetohydrodynamic (MHD) stability, (2) the description and causes of the observed MHD activity, and (3) the effect of the MHD activity on the confinement. Since the ISX-B experiment is an ongoing effort, definitive answers to all questions have not yet been found. However, a great deal of progress has been made in understanding some of these problems, and we will present here the current perception of what the answers are. In addressing such questions we have had to (1) carefully model ISX-B discharges, (2) develop further the theoretical understanding of the MHD instabilities, and (3) perform detailed comparisons between the experimental results and the three-dimensional (3-D) numerical simulations (Fig. 1). We will first describe the basic experimental and theoretical tools used in such studies.

Mirnov coils and collimated soft x-ray detectors are used for instability diagnostics. The former yield poloidal field fluctuations $\tilde{B}$ at 3 to 5 cm into the shadow of limiters, and the latter yield line-integrated measurements of x-ray emission fluctuations $\tilde{X}$ along viewing chords through the plasma. Up to 32 coils in a single poloidal cross section are used simultaneously for determining the poloidal mode number m of the poloidal magnetic field fluctuation $\tilde{B}$. A few other coils are available at two other locations around the torus for determining the gross toroidal mode number n. The x-ray studies use various combinations of detectors in a 32-unit fan array centered on the outside equatorial plane and in two 24-unit fan arrays mounted on top (Fig. 1). The lines of sight of all three arrays are in the same poloidal section.

The frequency response of most of the coils rolls off above 8 kHz due to the L/R for magnetic diffusion through their protective cases. A few special loops at the outside of the torus at only one toroidal location have rolloffs at $\gtrsim$125 kHz. The x-ray detectors have bandwidths of $\gtrsim$125 kHz. Instability signals from all channels are dominated by frequencies in the 5- to 25-kHz range. Data acquisition is both oscillographic and digital. The latter system evolved to 88 channels and is usually operated at a digitizing rate of 170.61 kHz for acquisition during a preselected 48-ms interval of individual tokamak discharges when attention is focussed on $\omega < 50$ kHz or at 512 kHz for a 16-ms interval for higher frequencies.

For the high-beta theoretical studies, we have used a reduced set of resistive MHD equations [5] valid in the limit of large aspect ratio ($\varepsilon \equiv a/R_o << 1$, where a and R_o are the plasma minor and major radii, respectively) and high beta ($\beta \sim \varepsilon$). This system of equations, with some minor variations, has also been used by other groups [6,7] for similar studies.

The reduced set of equations in dimensionless form is

$$\frac{\partial \Psi}{\partial t} + \vec{v}_\perp \cdot \vec{\nabla}\Psi = \frac{-\partial \Phi}{\partial \zeta} + \eta J_\zeta - E_{\zeta w} \tag{1}$$

$$\frac{\partial U}{\partial t} + \vec{v}_\perp \cdot \vec{\nabla} U$$

$$= S^2 \left[\frac{1}{R} \hat{\zeta} \cdot (\vec{\nabla} J_\zeta \times \vec{\nabla}\Psi) - \frac{1}{R^2} \frac{\partial J_\zeta}{\partial \zeta} + \frac{\beta_o}{2\varepsilon^2 R} \hat{\zeta} \cdot (\vec{\nabla} \times R^2 \vec{\nabla} p) \right] \tag{2}$$

$$\frac{\partial p}{\partial t} + \vec{v}_\perp \cdot \vec{\nabla} p = 0 \tag{3}$$

with

$$U = \nabla_\perp^2 \Phi \tag{4}$$

and

$$J_\zeta = \Delta^* \Psi = R^2 \vec{\nabla}_\perp \cdot \left(\frac{1}{R^2} \vec{\nabla}_\perp \Psi \right) \tag{5}$$

where R is the major radius coordinate divided by R_o, β_o is the toroidal beta at the magnetic axis, and $\hat{\zeta}$ is a unit vector in the toroidal direction. All lengths are normalized to the averaged minor radius a, the resistivity to η_o (its value at the magnetic axis), the time to the resistive diffusion time $\tau_r = a^2\mu_o/\eta_o$, the magnetic field to $B_{\zeta o}$ (the unperturbed vacuum toroidal field at major radius R_o), the velocity to a/τ_r, and the pressure to p_o (its value at the magnetic axis). The functions Ψ and Φ are the poloidal flux and velocity stream functions, normalized to $a^2B_{\zeta o}$ and $a^2B_{\zeta o}/\tau_r$, respectively. They are related to the dimensionless magnetic field and fluid velocity by

$$\vec{B} = \frac{\varepsilon}{R}\,\hat{\zeta} \times \vec{\nabla}\Psi + \frac{1}{R}\,\hat{\zeta} \tag{6}$$

and

$$\vec{v}_\perp = \vec{\nabla}\Phi \times \hat{\zeta} \tag{7}$$

where the subscript $\perp$ denotes perpendicular to $\hat{\zeta}$. The toroidal current density is J_ζ/R, normalized to $B_{\zeta o}/\mu_o R_o$, and U is the toroidal component of the vorticity. The parameter S is the ratio of the two time scales involved in this problem: $S = \tau_r/\tau_{hp}$, where τ_{hp} is the poloidal Alfvén time, $\tau_{hp} = R_o(\mu_o\rho_m)^{1/2}/B_{\zeta o}$. A conducting wall boundary condition is assumed, along with zero pressure, at the plasma edge. We use a straight magnetic field line coordinate system, (ρ,θ,ζ), where ρ is a flux surface label, $0 \leq \rho \leq 1$; ζ is the previously defined toroidal angle; and the poloidal angle θ coordinate is determined by requiring that the Jacobian is proportional to R^2.

For an axisymmetric, zero-velocity equilibrium, Eqs. (1) to (5) become

$$\eta J_\zeta = E_{\zeta W}$$

$$J_\zeta = -\frac{\beta_o}{2\varepsilon^2} R^2 \frac{dp}{d\psi} - F\frac{dF}{d\psi}$$

$$\Delta^* \psi = J_\zeta$$

which are the tokamak equilibrium equations exact to all orders in ε. Therefore, Eq. (2) contains the equilibrium magnetic field curvature terms to all orders in ε.

The implementation of these nonlinear equations as an initial value problem constitutes one of the time-stepping modules, RST [8], of the Oak Ridge National Laboratory (ORNL) MHD system of codes. This system of codes consists of three types of modules: input modules, time-stepping modules, and output modules. The third type includes mainly diagnostic codes. They have been used to improve the understanding of the instabilities studied. They are excellent tools for unraveling some of the characteristics of the basic dynamic mechanisms. Some output modules are used to calculate quantities, such as x-ray emissivity profiles and x-ray traces, that can be directly compared with experimental data (Fig. 1).

For resistive ballooning mode studies we have used two different types of codes: 1) a one-dimensional (1-D) shooting code, which assumes incompressibility but does not assume large aspect ratio and 2) a 1-D initial value code based on the reduced set of resistive MHD equations in the large n limit, which can incorporate effects such as parallel dynamics, ω_{*e}, viscosity, etc. Both modules use as input the same numerical equilibrium as RST.

Section II briefly describes the ideal MHD stability studies. Section III presents the experimental MHD activity observations. Sections IV and V discuss the $n = 1$ dominated discharges and discharges in which $n = 1$ activity is not present. Finally, the possible MHD-induced transport effects are discussed in Sect. VI.

II. IDEAL MHD STABILITY STUDIES

The ideal MHD stability studies have required a careful reconstruction of the ISX-B equilibria [9]. These equilibria have been calculated using the data analysis code ZORNOC [10]. This code requires as input the plasma geometry parameters (major radius, minor radius, elongation, and triangularity) which are obtained from the poloidal magnetic measurements [11]. With this information providing the boundary conditions, an equilibrium is calculated using the experimental pressure profile and an assumed current profile. The pressure profile is obtained from the midplane Thomson scattering and ion temperature measurements supplemented by neoclassical ion power balance and beam slowing down equations. The shape of the current profile is then varied to fit the measured poloidal coil currents, the magnetic field measurements, and the location of the $q = 1$ surface suggested by the soft x-ray diagnostic. Several equilibria, with β_p ranging between 1 and 2, have been found which closely match all experimental data. These equilibria were tested for ideal MHD stability using the ERATO code [12] for low toroidal mode number n and the MBC code [13] for large n. For low n, the complexity of the numerical calculation precludes the use of enough grid points to calculate a converged growth rate. Thus, extrapolation to zero spacing between grid points is necessary to assess stability. In Fig. 2(a), a plot of the squared growth rate is shown versus N^{-2}, where N is the number of grid points. This extrapolation shows marginal stability for the low n mode, within the accuracy of the present numerical studies. This has consistently been the result for all ISX-B equilibria studied.

For a few cases, the second most unstable mode has been studied. These modes were also found marginally stable by the same extrapolation procedure. This suggests an accumulation point at zero growth rate and is under further study. The growth rates are independent of the location of a conducting wall since the unconverged modes are localized within the $q = 1$ surface (for $n = 1$) or close to the $q = 1$ surface (for higher n). (The $q = 1$ surface for ISX-B equilibria is typically at $r/a \sim 1/3$ and thus in a region which is not affected by edge stabilization.) All equilibria were found to be stable in the infinite

n limit but close to marginal stability. Raising the pressure uniformly by ~30% was sufficient to cause destabilization in what was initially the most stable case.

In conclusion, all the ISX-B equilibria studied at present show marginal stability to low n ideal MHD modes within the accuracy of the calculation. The equilibria are stable to high-n modes but close to marginal. These results modify some results previously presented [14] that indicated that the high-beta ISX-B equilibria were ideal MHD unstable. The main reason for the change is the more accurately calculated equilibria in the present studies. The most pronounced difference is in the toroidal current distribution. As can be seen in Fig. 2(b), the current distribution has shoulders, which are generally more pronounced for the smaller values of q_ψ (the safety factor at the plasma edge).

III. DESCRIPTION OF THE OBSERVED MHD ACTIVITY IN ISX-B

In this section we review the main features of the MHD activity observed experimentally in ISX-B. We begin by describing the frequency spectrum of the Mirnov coil signals. Three characteristic observations follow:

(1) A clear peak at frequencies between 5 and 25 kHz (depending on the parameters of the discharge) with higher harmonics often present [Fig. 3(a)]. The peak corresponds to the n = 1 mode and dominates the spectrum when there is a significant plasma volume within the q = 1 surface, as is usually the case.

(2) A high-frequency tail, resolvable out to 250 kHz. These fluctuations are present independent of the n = 1 mode [Fig. 3(b)]. The amplitude level increases with beam injection, and the poloidal correlation lengths are typically on the order of 5 cm.

(3) At times, highly coherent structures in the tail, generally between 100 and 200 kHz. For at least some of these there is evidence that they are present for only brief intervals during the discharge.

For the n = 1 dominated discharges, the instability signals are altered when the ratio of injected beam power to ohmic power exceeds one. The changes are first marked by the lengthening of the interval of m = 1 activity before the internal disruption and the simultaneous appearance of a strong poloidal magnetic field fluctuation $\tilde{B}$ at the same frequency as the m = 1 [Fig. 4(a)]. Thereafter, the visual appearance of the instability patterns (i.e., of the envelopes of the oscillatory components $\tilde{X}$ and $\tilde{B}$) varies with plasma parameters. Generally, further increases in beam power lead first to longer-lived, even steadily running precursors and then to increasing amplitude modulation of these signals. Under some conditions the appearance of a long period sawtooth is retained and in other cases it is not.

These signal patterns are illustrated by the $\tilde{X}$ traces shown in Fig. 5, which gives samples for plasmas with dominant (m = 1;n = 1) mode activity ($q_\psi < 4.5$). The $\tilde{B}$ envelopes look like these as well since once the $P_b/P_{OH} \gtrsim 1$ threshold is exceeded, the $\tilde{B}$ and $\tilde{X}$ signals are locked in frequency and in amplitude. The rapid modulation pattern shown as the final example in Fig. 5(c) looks quite similar to signals

from "fishbone" activity in the Poloidal Divertor Experiment (PDX) [15]. Signals like these are rare in ISX-B and no particular confinement deterioration is associated with them. With regard to the general nature of signals from ISX-B, we note that operation with deliberately shaped (elliptical) plasma favors the more continuous $\tilde{X}$ and $\tilde{B}$, and the patterns revert toward those of the classic sawtooth (or, equivalently, toward patterns typical of lower P_b) as q_ψ is increased.

Despite the variation of signal patterns with plasma parameters, the basic features of these signals do not vary once the $P_b/P_{OH} \gtrsim 1$ threshold is passed. $\tilde{X}$ and $\tilde{B}$ signals are locked at the same frequency and coupled in amplitude. The $\tilde{B}$ at the Mirnov coils is strong, often exceeding $\tilde{B}/B = 1\%$, and is dominated by $(m = 2; n = 1)$ mode symmetry at low q_ψ and by mixtures of m at higher q_ψ. The $\tilde{B}$ measurements indicate that the mode rotation is reversed from that in ohmically heated plasmas, presumably the result of toroidal rotation driven by momentum transfer from the co-injected neutral beams [16]. The large $\tilde{X}$ signals are from within $q \simeq 1$ and are due to a large $m = 1$ mode there. Rotation of this $m = 1$ structure is also reversed. Even with a large $(m = 2; n = 1)$ poloidal field signal, there is no large or distinctive $\tilde{X}$ from near $q = 2$ and thus no large $m = 2$ island structure. The $\tilde{X}$ waveforms do show interesting differences of detail when compared with the work of others [17] on the classic $m = 1$. We illustrate these details in the next section.

We now turn our attention to the high frequency tail signals. We have not yet obtained experimental mode identifications for these. The high-frequency tail in $\tilde{B}$ can be adequately observed only on those Mirnov coils with the higher frequency response. A variety of tests confirm that this tail is indeed due to magnetic field fluctuations. It is unlikely that the source is plasma local to the coils since comparisons have been made between the signals of the high frequency coils and those from a Langmuir probe which was located at the same minor radius and poloidal angle as one of the coils and only 5 cm away toroidally. The high-frequency spectra are similar, but the coherence between $\tilde{B}$ and $\tilde{n}$ is zero. Furthermore, the time histories of $\tilde{B}$ and $\tilde{n}$ throughout a discharge are totally different.

As noted in connection with Fig. 3, the high frequency tail in $\tilde{B}$ is present with or without a strong (m = 1;n = 1) mode. The signal levels increase markedly with neutral beam injection. The fact that this increase is not due to a shift of the bulk plasma outward (and thus closer to the high frequency coils) was demonstrated by experiments directed specifically at this question. The time response of the amplitude increase is similar to that of β_p (Fig. 6). The signal level follows β_p even before injection when β_p increases due to a density increase produced by strong gas puffing [Fig. 6(a)]. The general amplitude level of the $\tilde{B}/B_p$ tail increases relatively systematically with beam power (β_p) in the ISX-B power scan, at fixed plasma current (I_p), toroidal field, and density (Fig. 7). However, the systematics of the variation of $\tilde{B}/B_p$ with β_p when the latter is controlled by I_p is not so clear (Fig. 8, with the I_p scan at fixed B_T, n_e, and P_b = 1 MW). A smaller range of β_p is allowed by this method, and the tail is augmented by pronounced bands of the more coherent activity, particularly at low I_p.

Since the high frequency coils are presently placed at only one toroidal location, it has not been possible to address the question of toroidal mode numbers for the high frequencies. We have approached the question of poloidal mode numbers, through calculation of cross power spectral densities (CPSD). This procedure develops "average" phase relations for the 16-ms data strings. The results are confused by the appearance of the more coherent bands. We are in the process of applying digital filtering codes to identify the time intervals when these signal components are present.

The high frequency tail also exists in the spectra of signals from the collimated x-ray detectors. These high frequencies are also present both with and without a strong (m = 1;n = 1) mode (Fig. 9). We have attempted, without success, to obtain local characterizations of the plasma by calculating CPSD for detectors whose lines of sight intersect in the plasma. Two difficulties arise. The (m = 1;n = 1) mode and its harmonically related driven structures usually dominate the detector signals; because of the long range correlations of these signal components they also dominate the coherence spectrum, even in the cases of detector pairs whose lines of sight do not intersect in

the plasma. When the technique is applied to discharges without the ($m = 1; n = 1$) mode, the coherence is low and noisy. Much more signal averaging than was possible in these experiments (effectively, about 50 samples) would be required to show any enhancement of coherence levels by including a plasma region common to the two lines of sight.

IV. n = 1 DOMINATED MHD ACTIVITY

Having presented the summary of experimental MHD observations in ISX-B in the previous section, we will now address the question of interpretation from the theoretical point of view. We start by considering in this section the situation in which the n = 1 instability is dominant. The high-frequency tail is considered in the next section. As noted in the introduction, the theoretical studies have been done in the framework of the resistive MHD model. Full details can be found in the literature [2,18]. To understand, in a systematic way, the change of the instability character with the parameters of the theory, model equilibria have been considered. With these equilibria we do not attempt to make a detailed match to ISX-B equilibria but rather try to understand the general change of features of the instability when beta increases. In order to separate the beta effects of the dynamic pressure-driving terms from those of the beta-induced changes in equilibrium, linear calculations were carried out in two ways: (1) using linearized versions of the resistive MHD equations and (2) using the same equations with the dynamic pressure term in the momentum balance Eq. (2) turned off. In the first method, pressure-driven and current-driven effects are included, whereas the second method allows for only current-driven effects. Beta effects observed using the second method of calculation are caused by the distortion of the equilibrium geometry, whereas the first method also includes the dynamic effects of the pressure terms.

As an example we discuss here a flux-conserving equilibrium sequence characterized by a pressure profile $p = p_0\psi^2$ and a safety factor profile $q = 0.9[1 + (\rho/\rho_0)^4]^{1/2}$, with $\rho_0 = 0.65$. For this equilibrium sequence, the most unstable mode at low beta is the n = 1 mode, and its linear stability properties with increasing beta are summarized in Fig. 10. In this figure we have plotted the n = 1 linear growth rate as a function of β_p.

The dashed curve was calculated without dynamical pressure effects and thus illustrates those changes in stability of the current-driven modes caused by equilibrium effects. The shift of the peak of the toroidal current relative to the magnetic axis (Fig. 11) decreases the average current gradient at the $q = 1$ surface and increases the couplings to other modes, which are stable. Both effects tend to stabilize the $n = 1$ mode. The solid curve in Fig. 10 includes pressure-driven dynamical effects in addition to those effects which lead to the dashed curve. For low values of β_p, the pressure terms produce an interchange stabilization of the $n = 1$ mode similar to that predicted by Glasser et al. [19], but as β_p increases, the character of the mode changes, becoming mainly pressure driven with an increasingly large growth rate.

The effect of beta upon the linear $n = 1$ eigenfunction is illustrated in Fig. 12, which shows the $(m = 1; n = 1)$ Fourier components of the poloidal flux function Ψ, the pressure p, and the velocity stream function Φ for different values of β_p. For $\beta_p = 0.19$ the ψ_{11} component is dominant and has the typical kink mode structure obtained in the low-beta limit, indicating that the $n = 1$ eigenmode is mainly a current-driven mode. At $\beta_p = 1.94$ the $n = 1$ mode is mainly pressure driven and its Fourier components are localized near the $q = 1$ singular surface. This particular equilibrium is stable to the $n = 1$ mode when the pressure-driving term is removed from the momentum balance equation, as indicated by the dashed curve of Fig. 10. For $\beta_p = 1.00$, Fig. 12 shows the transition from current- to pressure-driven dominance.

A large number of Fourier components is necessary to correctly describe an eigenmode when the beta effects are included. We have determined that the coordinate system which we use is optimal in minimizing the number of components. Even so, about ten poloidal components are required to calculate the linear growth rates accurately to within a few percent. In Fig. 13, we show the different poloidal components of Ψ used in calculating the linear $n = 1$ eigenmode for $\beta_p = 0.19$. All modes show a global character like the $(1;1)$ component in Fig. 12 for this value of β_p. The $m = 2$ component is the largest of the driven components, and its structure is quite different from a

linearly unstable (m = 2;n = 1) tearing mode. This driven m = 2 component peaks near the q = 1 singular surface and has hardly any structure near the q = 2 surface. This feature of the m = 2 component carries over into the nonlinear regime, with important observable consequences. At the highest value of β_p considered (β_p = 2), the structure of the components is considerably different, as was already seen for the (m = 1;n = 1) in Fig. 12. All components are highly localized near the q = 1 surface, the m = 1 component is no longer the dominant one, and the character of the mode is totally different.

In summary, β_p modifications to the n = 1 linear mode are induced by distortion of the equilibrium current profile, which changes the growth rate and couples components having different m values, and by the transition from current to pressure as the driving term of the instability.

To compare these results with experimental observations we have to study the nonlinear evolution of such instabilities. We limit the comparison to low and moderate beam injection powers (moderate values of β_p). At higher β_p values, the theoretical model has some limitations in adequately describing the (m=1;n=1) mode. A potential problem is that the ideal internal kink can be unstable at such β_p values and the accurate description of this mode requires higher order terms in ε. Present calculations with the ERATO code show that for all ISX-B equilibria studied this mode is close to marginal stability, but we have not yet attempted to do a detailed nonlinear calculation for the (m=1;n=1) mode at high β_p. Theoretical considerations aside, the experimental observations indicate that the spatial structure of the (m=1;n=1) activity does not change with increasing β_p.

The main results of the nonlinear numerical studies [18] can be summarized as follows:

(1) For the flux-conserving equilibrium sequence considered in this paper and $\beta_p \lesssim 0.5$, the nonlinear growth of the m = 1/n = 1 magnetic island slows down with increasing β_p, going from exponential to linear prior to reconnection (Fig. 14).

(2) For higher values of β_p, the m = 1/n = 1 magnetic island saturates and remains at a finite amplitude. This transition from

reconnection to saturation happens when the mode becomes dominantly pressure driven.

(3) The (m = 1;n = 1) mode drives, through toroidal and nonlinear coupling, many modes. The driven mode with the largest amplitude for this equilibrium sequence is the (m = 2;n = 1) mode. This mode, as discussed above, is mainly localized near the q = 1 surface. The m = 2/n = 1 magnetic island induced near q = 2 is small, and hence only a small $\tilde{X}$ signal is produced there. However, the (m = 2;n = 1) mode produces a large poloidal magnetic field perturbation at the plasma surface.

(4) The broad mode spectrum driven by the (m = 1;n = 1) mode generates a variety of magnetic islands that in many cases overlap and break the magnetic surfaces. This complex mode structure is illustrated in Fig. 15, which shows snapshots of the magnetic field structure slightly before magnetic field line reconnection, taken at four different toroidal locations.

(5) As q at the edge is raised, the instability reverts toward the classical low-beta m = 1 mode. Growth of the m = 1 island speeds up due to increasing shear at the q = 1 surface, and the amplitudes of the driven modes and $\tilde{B}$ at the limiter decrease because the radius of q = 1 is reduced.

These results of the theory and the gross features of the experimental observations described in the previous section are clearly in agreement. A comparison at a more detailed level results from calculating model $\tilde{X}$ waveforms for the theoretically predicted mode structure. In these studies, we used equilibria which closely model ISX-B experimental results, as described in Sect. II. The nonlinear evolution was followed in time. The $\tilde{X}$ along various chords at different times were calculated as line integrals of p^2 assuming toroidal rotation of the mode structure at a constant frequency ω. A comparison of experimental and model waveforms for the side-mounted array is given in Fig. 16. The latter resulted from co-rotation of the instability structure shown in Fig. 15. Features of dominant m = 1 are evident in both displays. There are additional fine-grained details common to both: (1) The channel nearest the center shows the expected dominant 2ω resulting from the m = 1. Successive peaks at the center

are not of equal amplitude, a feature that in the model calculation results from the presence of the driven m = 2 rotating in phase with the m = 1. (2) The double humps on positive half-cycles at nearby channels (e.g., 15 and 17) are also not equal, and the order of the inequality reverses between upper and lower channels. These features are again the result of the m = 1 and m = 2 couplings. If counter-rotation is assumed in the model, the theoretical traces for channels 15 and 17 are exchanged and then disagree with the experimental traces. (3) At channels 10 and 22, the waveforms are triangular in nature and are again reverse imaged between upper and lower channels. This is just outside q = 1, where the (m = 1;n = 1) eigenfunction no longer dominates and so no longer obscures the effects of coherent superposition of all the other mode components. The assumption of counter-rotation leads to similar consequences in the case of channels 10 and 22. This combination of effects has been illustrated in Fig. 17. The modification of the $\tilde{X}$ waveform generated by a single (m = 1;n = 1) mode [Fig. 17(a)] due to the toroidal coupling of the (m = 2;n = 1) is shown in Fig. 17(b). The final result of superimposing the high-n driven modes is shown in Fig. 17(c). The resulting $\tilde{X}$ waveforms in Fig. 17(c) model quite closely the experimental waveforms. Furthermore, when a poloidal rigid rotation is applied to the calculated mode structure, the predicted x-ray waveforms are different from the toroidally rotated ones (Fig. 18) and do not agree with the experimental observations. This fact gives an indirect confirmation of the assumed dominance of the toroidal rotation in ISX-B.

As β_p is increased into the higher range obtained in ISX-B, the role of the $n > 1$ modes in the overall predicted mode structure becomes increasingly important. These modes are themselves linearly unstable and thus are no longer linked to the evolution of the (m = 1;n = 1). At very low resistivity, as in the experiment ($S > 10^6$), these $n > 1$ modes saturate at small amplitude, but their overall level is large enough to potentially influence transport. We shall discuss them in the next section.

V. n > 1 RESISTIVE PRESSURE-DRIVEN MODES

The resistive MHD calculations show that at finite beta, there are also unstable resistive pressure-driven modes [20], resistive ballooning modes [21-24], the saturated level of which increases with β_p. In the framework of the incompressible, resistive ($k_\parallel^2 v_T^2 < \omega\nu_{ei}$) MHD model (for $\beta_p > 1$ and below and near the critical beta for ideal instabilities), it has been found that the fastest growing mode, with a given toroidal mode number n, has a growth rate

$$\gamma_n \simeq \left(\frac{n^2\eta_{eq}}{S}\right)^{1/3}\left(\frac{\beta_o q^2}{\epsilon\rho L_p}\right)^{2/3}\tau_{hp}^{-1}$$

where $L_p = [(-dp/d\rho)/p(0)]^{-1}$ is a characteristic scale length for the pressure profile. The basic theory of these instabilities from an analytic point of view is discussed by P. H. Diamond [20]. Their properties are similar to the resistive interchanges [25,26]. However, the resistive ballooning modes are driven by geodesic curvature, not averaged curvature. They extend greatly along magnetic field lines, as can be seen by looking at the linear eigenfunction (Fig. 19), calculated by solving the resistive ballooning mode equation [n → ∞ limit of Eqs. (1) to (3)]:

$$\frac{\partial}{\partial y}\left[\frac{\alpha}{1 + (n^2\eta_{eq}/\gamma S)\alpha}\frac{\partial\phi}{\partial y}\right] - \left[\frac{\beta_o}{\epsilon}\frac{q^3}{\rho}\frac{dp_{eq}}{d\rho}\frac{\partial(qy + \delta)}{\partial Z} + q^2\gamma^2\alpha\right]\phi = 0 \qquad (8)$$

with

$$\alpha = \frac{q^2}{\rho^2}\left(g^{\rho\rho}\hat{s}^2 y^2 + 2g^{\rho\theta}\hat{s}y + g^{\theta\theta}\right)$$

The term $\partial(qy + \delta)/\partial Z$ contains the equilibrium magnetic field curvature term that, as mentioned in the introduction, is exact to all orders in ϵ. We express this term as

$$\frac{\partial qy}{\partial Z} = \frac{1}{\rho R}\left(q \frac{\partial X}{\partial \rho} - \frac{dq}{d\rho} y \frac{\partial X}{\partial y}\right)$$

where $X = X(\rho,\theta)$, $Z = Z(\rho,\theta)$ is the inverse equilibrium solution of the Grad-Shafranov equation. In the numerical calculations, we use a numerical solution of the equilibrium equation. However, it is useful to have a model equilibrium as a guide for analytic calculations. We take as a model the equilibrium described in the appendix of Ref. [27]. For this case

$$X = \epsilon a_0(\rho) + \rho \cos\theta + \epsilon a_2(\rho)\cos 2\theta$$

$$Z = \rho \sin\theta + \epsilon a_2(\rho)\sin 2\theta$$

which gives

$$\frac{\partial qy}{\partial Z} = \frac{q}{\rho}\left\{\epsilon \frac{da_0}{d\rho} + \cos y + \hat{S} y \sin y + \epsilon\left[-\rho + \left(\frac{da_2}{d\rho} - \rho\right)\cos 2y + \hat{S} y \left(\frac{2a_2}{\rho} - \rho\right)\sin 2y\right]\right\}$$

The averaged curvature term is given by $da_0/d\rho$ and for $q > 1$ is negative. Therefore, these resistive pressure driven modes cannot be driven by the averaged curvature; rather, they must be driven by the geodesic curvature [20]. The characteristic width along the magnetic field lines is obtained by solving Eq. (8) for large y:

$$W_n = [\langle g^{\rho\rho}\rangle q^4 \hat{S}^2 n^2 \gamma_n \tau_{hp}^{-1}/(\rho^2 S)]^{-1/4} \qquad (9)$$

The linear analytic results agree well with the numerical calculations. In real space, the different Fourier components of the linear eigenfunction, when calculated using the full 3-D MHD code, are strongly localized at the singular surfaces (Fig. 20), and the radial width Δ, which can be calculated using the reciprocity of y (ballooning space) and position space, is given by $\Delta \propto (nq\hat{s}W_n/\rho)^{-1}$.

The numerical calculations of the linear growth rate using the 3-D MHD equations agree with the predictions of the ballooning equation (8), even for very low values of n (Fig. 21). Finite aspect ratio corrections do not modify this result. Therefore, the large n equations contain, within the limitations of the model, all the physics of these modes and are a useful tool for analytical calculations.

Using the nonlinear resistive MHD equation in the ballooning representation, a calculation of the renormalized response has been performed [20]. This calculation shows that the dominant nonlinear effect is due to the pressure convective nonlinearity, which reduces the turbulent pressure response of $\tilde{p}$ due to $\tilde{\phi}$, the electrostatic perturbation. This causes a reduction of the interchange destabilizing term without changing the basic structure of the eigenfunction. A physical interpretation is that the resistive ballooning modes saturate when the pressure fluctuation mixes $dp/d\rho$ over the radial extent Δ of each poloidal subharmonic; thus, $\tilde{p} \propto \Delta\, dp/d\rho$. Since the pressure is mainly convected, we have $\tilde{p} \propto [inq\tilde{\gamma}(dp/d\rho)]/(\rho\gamma_n)$. Therefore, the kinetic energy of these modes at saturation is

$$E_K = \left\langle \left| \frac{nq}{\rho}\, \tilde{\gamma} \right|^2 \right\rangle \approx \Delta^2(\gamma_n \tau_{hp}^{-1})^2$$

$$= \left(\frac{\eta_{eq}}{S}\right)^{-4/3} \left(\frac{\beta_o}{\epsilon}\, q^2\, \frac{1}{L_p}\right)^{5/3} \qquad (10)$$

It is apparent from this result that the saturated level of these modes increases with β_p. We have numerically studied, with the 3-D code RST, the nonlinear evolution of many modes. We have used up to 81 Fourier components with values of n up to 11. For these studies we chose a sequence of flux-conserving equilibria for which the q profile does not

include the q = 1 and q = 2 surfaces. Thus, the (m = 1;n = 1) mode and its driven activity do not interfere with the nonlinear evolution of resistive ballooning modes. The equilibria are also required to be ideal MHD stable. We have observed the saturation of the total kinetic energy of these modes (Fig. 22) and confirmed the scaling with β_p and S of their saturated level. It is important to notice that S has to be greater than or equal to 10^5 to compare the numerical calculations with the predicted saturation level given by Eq. (10). If S is smaller (i.e., if the resistivity is very large), the character of the modes changes and they become localized along the field lines (Fig. 19). Their linear growth rate is large and weakly dependent on the resistivity. The instability is in this case similar to the fast resistive interchange of Coppi et al. [26]. These modes have a larger nonlinear saturation level than that given by Eq. (10). We can also estimate the level of magnetic fluctuations at saturation by using the saturated value of $\tilde{\phi}$ given by Eq. (10) and using the linear relation

$$\left(\gamma_n + \frac{n^2 \eta_{eq}}{S}\,\alpha\right)\tilde{\psi} = \frac{1}{q}\,\frac{\partial \tilde{\phi}}{\partial y}$$

We find that

$$\frac{\tilde{B}_p}{B_p} \cong \left(\frac{\eta_{eq}}{S}\right)^{1/3}\left(\frac{\beta_o}{\varepsilon}\,q^2\,\frac{1}{L_p}\right)^{7/6} \tag{11}$$

which indicates that the magnetic fluctuations within the plasma increase with β_p. This increase of magnetic fluctuation in the plasma would probably show up experimentally as an increase on the signal at the Mirnov coils with β_p.

The 3-D numerical calculations also give the n spectrum for these modes (Fig. 23). The spectrum shows a slow falloff with n. This is contrasted in Fig. 23 with the n spectrum when the n = 1 mode dominates. Though the association must be regarded as conjecture at this time, the slow falloff of the n spectrum may be related to the high-frequency tail observed in the experiment. The notion here is

that the higher mode numbers are Doppler shifted to higher frequencies, so the slow falloff in n leads to a slow falloff in the experimental spectra.

The reduced set of MHD equations does not contain all the physics necessary to fully understand the theory of the instabilities we consider here. Such effects as compressibility [22] and ω_* are known to be stabilizing for the resistive ballooning modes. P. H. Diamond [20] gives a detailed treatment of ω_* effects.

We can relax the incompressibility condition by including the parallel dynamics terms in the ballooning equation. This introduces a stabilizing effect on the resistive ballooning modes. The ion sound effects undercut the destabilizing pressure and the linear dispersion relation becomes

$$\gamma^3 + \omega_S^2\gamma = \gamma_n^3 \tag{12}$$

where γ_n is the linear growth rate for the incompressible limit given before and $\omega_S = v_s/(qR)$ is the sound frequency. From Eq. (12) it is clear that the growth rate weakens and its power dependence on the resistivity changes from 1/3 to a value between 1/3 and 1. This stabilizing effect is negligible for modes such that

$$n > \frac{S^{1/2}\varepsilon\rho L_p}{\beta_o^{1/4}q^{7/2}}\left[\frac{p(\rho)}{p(0)}\right]^{3/4} \tag{13}$$

which, for high-β_p discharges in ISX-B, implies $n \gtrsim 5$. Numerical calculations using the resistive ballooning equations with parallel dynamics terms included agree with these estimates (Fig. 24). The reason that the effects of the parallel dynamics are limited to very low n values in high-β_p ISX-B plasmas is as follows: (1) the electron temperature of the outer half of the plasma is low ($T_e \lesssim 200$ eV) and (2) the high-β_p discharges have been achieved by operating at low plasma current (high q_ψ). To see this better we give in Table I the

values of ω_s, ω_{*e}, γ_n, and W_n for four typical ISX-B discharges at two-thirds of the minor radius (center of the confinement region).

These instabilities could explain the high-frequency fluctuations observed in the experiment. The presence of the fluctuations when the $n = 1$ is absent supports this interpretation. Moreover, we can calculate the $\tilde{B}_p$ autocorrelation function as a function of radial, poloidal, and toroidal separation (Fig. 25) at the plasma boundary when the modes are saturated, and the typical poloidal correlation length turns out to be on the order of 5 cm, which is in agreement with measured poloidal coherence length for the high-frequency tail in $\tilde{B}_p$. The evidence cited earlier for increasing $\tilde{B}$ with increasing β_p lends further support, although a detailed quantitative comparison cannot be made because we have not yet calculated the frequency spectrum for these modes. The problem is further complicated by the highly sheared toroidal rotation velocity in ISX-B, which depends on the power input. In the case of the I_p scan, at fixed power, there is possibly no significant change of toroidal rotation, which simplifies the problem. However, the presence of the $n = 1$ mode at high current distorts the low-frequency part of the spectrum, and the high-frequency tail is deformed at low current by the appearance of the coherent structures discussed in the previous section. These make it impossible to detect a change of the saturated level by the factor of about 3 expected from Eq. (11). However, the high-frequency structures observed at low current which have long correlation lengths could be associated with the lower-n modes being destabilized when q increases [see Eq. (13)].

VI. EFFECT OF THE MHD ACTIVITY ON CONFINEMENT IN ISX-B

A deterioration in confinement is observed in ISX-B discharges [1,4,28] with high neutral injection power at high β_p. The present experimental results alone do not permit us to identify whether the cause of the confinement deterioration is due to the heating method ($\tau_E \propto I^{3/2} P_b^{-2/3}$) or is intrinsic to high-β_p plasmas ($\tau_E \propto I^{1/2} \beta_p^{-2}$) or both. A possible cause of this deterioration, linked to high β_p, is the MHD activity.

The role of the (m = 1;n = 1) mode (and the other activity which it drives) in the energy confinement has been studied experimentally by toroidal magnetic field and plasma current scans [2,3,28]. In the case of B_T scans, for instance, at fixed plasma current and density, raising q_ψ reduces the intensity of the (m = 1;n = 1) and driven modes and presumably any associated losses. Such scans at P_b = 0.6 MW and $P_b \approx 2.0$ MW lead to no change in confinement time (Fig. 26). It is then concluded that the (m = 1;n = 1) mode and its driven activity are not the sole cause of the pronounced degradation of confinement observed in ISX-B. However, the resistive ballooning modes provide a possible explanation.

This is not to say that the (m = 1;n = 1) mode and its driven activity do not play any role in the deterioration of transport at high beta. We claim that they are not the dominant causes for such deterioration. As q_ψ increases in the toroidal field scan, the region of the plasma affected by the (m = 1;n = 1) mode and its driven activity decreases; at the same time the region affected by the resistive ballooning modes increases. Probably the net result is that one effect balances the other. Due to the complex magnetic structure generated by the (m = 1;n = 1) mode (regions with good surfaces, islands, and stochastic magnetic field line regions, see Fig. 15), it is very difficult to make an analytic estimate of its induced transport effects. However, for the resistive ballooning modes such an estimate can be achieved. Using the analytic model for the saturation of the resistive ballooning modes [Eq. (10)], an estimation can be made of the induced losses [20,27]. It is found that convective losses are negligible and the dominant loss channel is the electron conduction.

We can calculate the magnetic field line diffusion coefficient D_M by constructing the renormalized theory for a zero-frequency electron drift kinetic equation with magnetic nonlinearity appropriate for toroidal systems. We use the calculated saturation level for the fluctuations and estimate the electron conductivity $\chi_e \cong v_{Te} D_M$. This lands to

$$\chi_e^{TH} \cong \frac{3}{2} (v_{Te} a) q \frac{1}{2} \left(\frac{\beta_o}{\epsilon} \frac{q^2}{\hat{s}} \frac{1}{L_p} \right)^{3/2}$$

Theoretical predictions based on the present model compare favorably with the results of the ISX-B beta-scaling experiments [27]. The points of agreement between the experiment and the theory are (1) electron heat conduction is the dominant loss channel at the high values of β_p obtained in the experiment with high-power neutral beam injection, and (2) the theoretical predictions of the electron thermal diffusivity (χ_e^{TH}) agree well over a large range of parameter variations with the values and shape of the experimental thermal diffusivity

$$\chi_e^{EX}(\rho) = \frac{P_{be} + P_{OH} - P_{ei} - P_{rad} - \frac{5}{2} T_e \Gamma_e A_\rho}{\frac{n_e A_\rho}{a} \left| \frac{\partial T_e}{\partial \rho} \right|}$$

based on the power balance considerations as discussed in Ref. [29].

The radial dependence of χ_e^{EX} is conveniently described by a three-plasma-region model: (1) a central core region [$\rho < \rho(q = 1)$] dominated by the $m = 1/n = 1$ mode and its driven modes [2]; (2) a confinement region outside the core, where a large pressure gradient is sustained; and (3) a plasma edge region ($\rho \gtrsim 0.8$), dominated by atomic physics effects and/or recycling of plasma particles. As long as the central core region is not too large (which is the case for ISX-B plasmas with $q_\psi > 2.5$) and the plasma is clean, heat conduction in the confinement region determines the confinement. Indeed, we observe that $1/\chi_e^{EX}$ in the confinement region correlates well with τ_{Ee}, the electron

energy confinement time, which in turn correlates with global energy confinement time. Since the global confinement time for high-power injection plasmas in ISX-B scales differently from that in ohmic discharges [3], it is not surprising that standard ohmic heating models of χ_e, all of which fit ohmic discharges reasonably well, do not come close to χ_e^{EX} in beam-heated, high-β_p discharges in either magnitude or scaling. On the other hand, the present theoretical model χ_e^{TH} fits closely the magnitude and shape of χ_e^{EX} over large parameter ranges. Figure 27 illustrates this agreement by directly comparing χ_e^{EX} and χ_e^{TH} for scans of plasma current (at P_b = 2 MW) and toroidal field (at P_b = 0.7 MW) [3]. In this figure, three χ_e values are given for the confinement region of each discharge, i.e., ρ = 0.50, 0.67, and 0.75; χ_e^{TH} agrees well with χ_e^{EX} over nearly two decades. Comparison of χ_e's in a larger ISX-B database indicates that the values from the theoretical model are much smaller than most experimental values at low β_p ($\beta_p < 0.9$). This is expected since the ballooning modes are reduced at low β_p, and competing processes could easily dominate confinement.

The electron thermal diffusivity has also been measured by applying the heat pulse propagation method [30] to sawtoothing discharges. For the ISX-B beam-power scan data, the resulting values [31] are like those from the power balance analysis previously described. They increase substantially as $P_b(\beta_p)$ increases from 0.3 to 2.0 MW (from β_p = 0.75 to 1.5). These results support the conclusion that the progressive degradation of confinement with increasing $P_b(\beta_p)$ is largely due to increasing electron thermal conduction.

The theoretically predicted χ_e^{TH} has been used in transport simulation of ISX-B discharges. With a constant multiplier equal to 2, the electron temperature profiles measured experimentally have been reproduced by these simulations. Details are given in Ref. [4].

VII. CONCLUSIONS

In this paper we have reviewed the MHD studies focused on the ISX-B tokamak that were performed over a two-year period. The studies have involved parallel efforts between experimental analysis of MHD activity, 3-D numerical simulation of ideal and resistive instabilities, and analytic modeling. The main results we have obtained are:

(1) The high-beta ISX-B equilibria are marginally stable to finite-n ideal MHD modes. The equilibria are stable to high n modes but close to marginal. These studies have required a careful reconstruction of the equilibria.

(2) The observed spectrum of MHD fluctuations in the ISX-B tokamak is clearly dominated by the $n = 1$ mode when the $q = 1$ surface is in the plasma. This fact agrees well with theoretical predictions based on 3-D resistive MHD calculations, valid for β below the threshold of the ideal internal kink mode. They show that the $(m = 1; n = 1)$ mode is the dominant instability. It drives other $n = 1$ modes through toroidal coupling and $n > 1$ modes through nonlinear couplings. These theoretically predicted mode structures have been compared in detail with the experimentally measured wave forms (using arrays of soft x-ray detectors). The agreement is excellent.

(3) The resistive MHD calculations also show that at finite beta there are unstable resistive pressure-driven modes. For low-β_p equilibria these modes saturate at very low levels and their evolution has little effect on the dominant $(m = 1; n = 1)$ mode. However, with increasing β_p they become more important. Their n spectrum is concentrated at low mode numbers and is broad, and analytic calculations indicate that their saturated kinetic energy scales like $(\varepsilon\beta_p)^{5/3}\eta^{4/3}$. These scalings have been confirmed by numerical results. These instabilities could be an explanation for the high-frequency fluctuations observed in the experiment. Further work is required in testing this hypothesis.

(4) The transport effects induced by the resistive ballooning modes have been estimated from the theory and found to be mainly thermal

electron conduction losses. An expression for χ_e has been derived, and it yields values that agree well with those from the experiment.

ACKNOWLEDGMENTS

We acknowledge with appreciation the support of our many colleagues in the ISX-B group and in the engineering staff. In particular, we acknowledge S. C. Bates, C. E. Bush, D. P. Hutchinson, C. H. Ma, G. H. Neilson, E. A. Lazarus, C. E. Thomas, and S. D. Scott for providing us with their diagnostic data. We also wish to thank H. C. Howe, M. N. Rosenbluth, M. J. Saltmarsh, and J. Sheffield for many useful discussions. This research was sponsored by the Office of Fusion Energy, U.S. Department of Energy, under contract W-7405-eng-26 with the Union Carbide Corporation and DE-FG05-80ET-53088 with the Institute for Fusion Studies.

REFERENCES

[1] SWAIN, D. W., et al., Nucl. Fusion 21 (1981) 1409.

[2] DUNLAP, J. L., et al., Phys. Rev. Lett. 48 (1982) 538.

[3] NEILSON, G. H., et al., submitted to Nucl. Fusion.

[4] WOOTTON, A. J., et al., paper presented at this meeting.

[5] STRAUSS, H. R., Phys. Fluids 20 (1977) 1354.

[6] MONTICELLO, D. A., PARK, W., JARDIN, S. C., CHANCE, M. S., DEWAR, R. L., WHITE, R. B., GRIMM, R. C., MANICKHAM, J., STRAUSS, H. R., JOHNSON, J. L., GREEN, J. M., GLASSER, A. H., KAW, P. K., RUTHERFORD, P. H., and VALEO, E. J., in Plasma Physics and Controlled Nuclear Fusion Research (Proc. 8th Int. Conf. Brussels, 1980) Vol. 1, IAEA, Vienna (1981) 259.

[7] EDERY, D., PELLAT, R., and SOULE, J. L., "Equations for the Nonlinear Evolution of Resistive Tearing Modes in Toroidal Plasmas," Report EUR-CEA-FC-1013 (1979).

[8] LYNCH, V. E., CARRERAS, B. A., HICKS, H. R., HOLMES, J. A., and GARCIA, L., Comput. Phys. Commun. 24 (1981) 465.

[9] WIELAND, R. M., CHARLTON, L. A., NEILSON, G. H., CARRERAS, B. A., DUNLAP, J. L., LAZARUS, E. A., LEE, D. K., MURAKAMI, M., and THOMAS, C. E., Bull. Am. Phys. Soc. 27 (1982) 924.

[10] WIELAND, R. M., et al., "A Pressure Profile Analysis of High β ISX-B Plasmas Using MHD Equilibrium Geometry," submitted to Nucl. Fusion.

[11] SWAIN, D. W., and NEILSON, G. H., Nucl. Fusion 22 (1982) 1015.

[12] GRUBER, R., et al., Comput. Phys. Commun. 21 (1981) 323.

[13] MOORE, R., "M.B.C., a Ballooning Stability Code for Finite Toroidal Mode Number," General Atomic Report GA-A16243 (1981).

[14] MUNRO, J., et al., Nucl. Fusion 22 (1982) 599.

[15] MCGUIRE, K., paper presented at this meeting.

[16] SUCKEWER, S., EUBANK, H. P., GOLDSTON, R. J., HINNOV, E., and SAUTHOFF, N. R., Phys. Rev. Lett. 43 (1979) 207.

[17] SAUTHOFF, N. R., VON GOELER, S., EAMES, D. R., and STODIEK, W., Paper C-5, in Proceedings of the IAEA Symposium on Current Disruption in Toroidal Devices (Garching, 1979), Max-Planck-Institut für Plasmaphysik Report IPP 3/51.

[18] HOLMES, J. A., CARRERAS, B. A., HICKS, H. R., LYNCH, V. E., and ROTHE, K. E., Phys. Fluids 25 (1982) 800.

[19] GLASSER, A. H., GREEN, J. M., and JOHNSON, J. L., Phys. Fluids 18 (1975) 875.

[20] DIAMOND, P. H., et al., paper presented at this meeting.

[21] FURTH, H. P., et al., in Plasma Physics and Controlled Nuclear Fusion Research (Proc. 2nd Int. Conf. Culham, 1964) Vol. 1, IAEA, Vienna (1965) 103.

[22] CHANCE, M. S., et al., in Plasma Physics and Controlled Nuclear Fusion Research (Proc. 7th Int. Conf. Innsbruck, 1978) Vol. I, IAEA, Vienna (1979) 677.

[23] BATEMAN, G., and NELSON, D. B., Phys. Rev. Lett. 41 (1978) 1804.

[24] STRAUSS, H. R., Phys. Fluids 24 (1981) 2004.

[25] FURTH, H. P., KILLEEN, J., and ROSENBLUTH, M. N., Phys. Fluids 6 (1963) 459.

[26] COPPI, B., GREEN, G. M., and JOHNSON, J. L., Nucl. Fusion 6 (1966) 101.

[27] CARRERAS, B. A., HICKS, H. R., and LEE, D. K. Phys. Fluids 24 (1981) 66.

[28] MURAKAMI, M., et al., paper IAEA-CN-41/A-4 in Plasma Physics and Controlled Nuclear Fusion Research (Proc. 9th Int. Conf. Baltimore, 1982), (to be published).

[29] CARRERAS, B. A., DIAMOND, P. H., MURAKAMI, M., DUNLAP, J. L., BELL, J. D., HICKS, H. R., HOLMES, J. A., LAZARUS, E. A., PARÉ, V. K., SIMILON, P., THOMAS, C. E., and WIELAND, R. M., "Transport Effects Induced by Resistive Ballooning Modes and Comparison with High β_p ISX-B Tokamak Confinement," to be published in Phys. Rev. Lett.

[30] SOLER, M., and CALLEN, J. D., Nucl. Fusion 19 (1979) 703.

[31] BELL, J. D., DUNLAP, J. L., PARÉ, V. K., CARRERAS, B. A., CALLEN, J. D., LAZARUS, E. A., THOMAS, C. E., and MURAKAMI, M., Bull. Am. Phys. Soc. 27 (1982) 924.

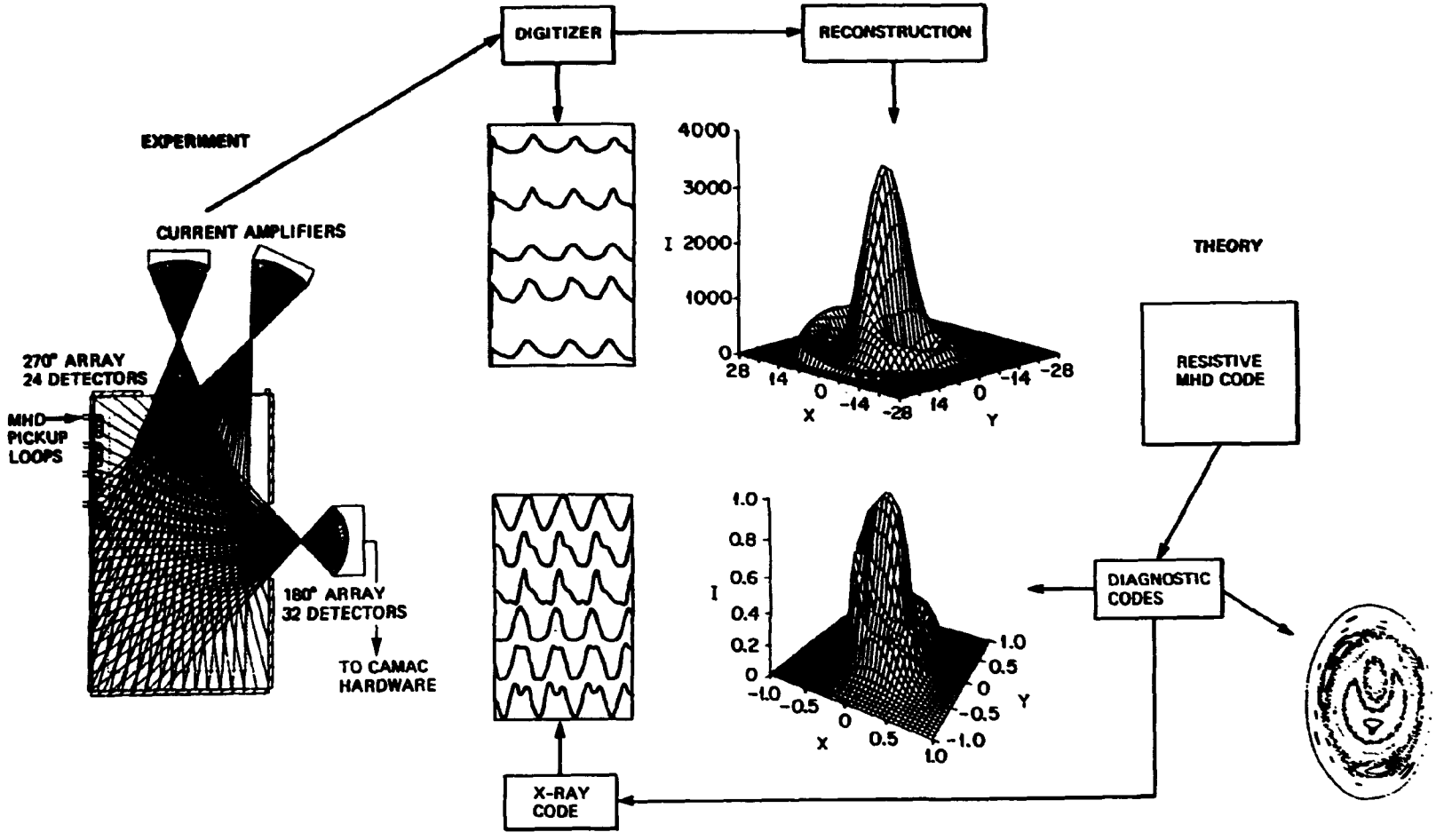

Fig. 1. Strategy for MHD studies at ORNL.

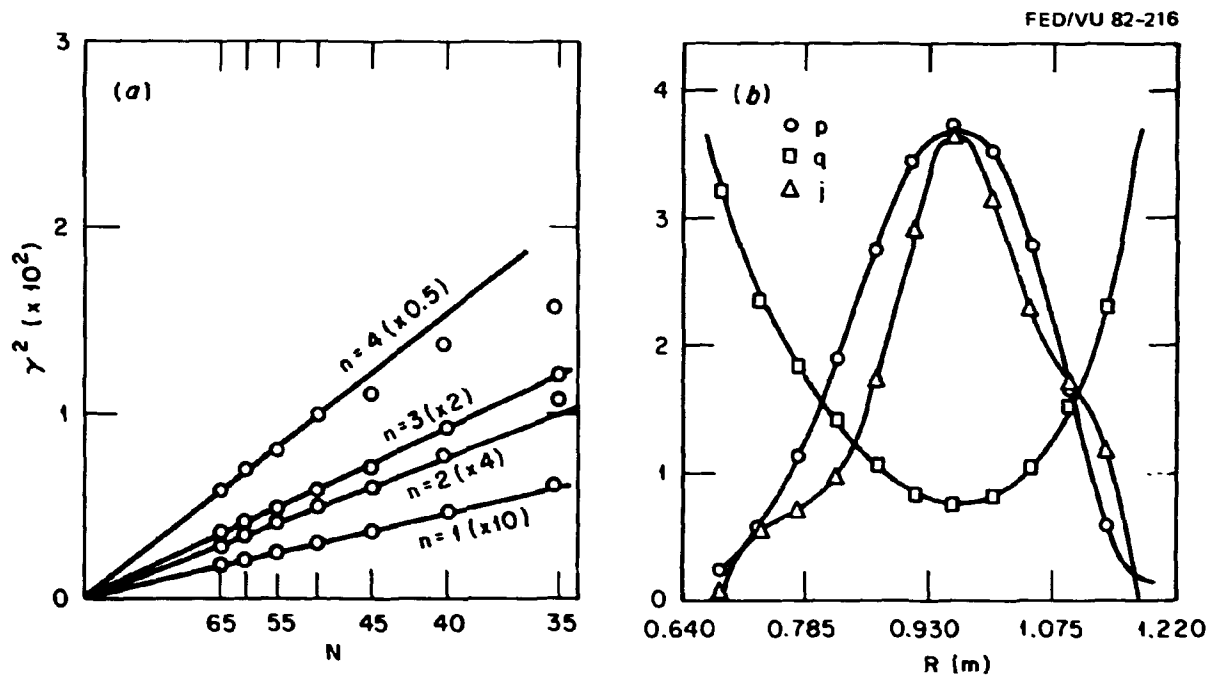

Fig. 2. (a) Growth rate squared (γ^2) vs the number of grid points used in the radial and poloidal directions. (b) The safety factor (q), pressure (p), and current density (j) for the $\langle\beta\rangle$ = 0.0253 case studied. Each curve is shown as a function of the major radius (R) at the midplane. The peaks of the pressure and current density profiles are normalized to the safety factor at the edge.

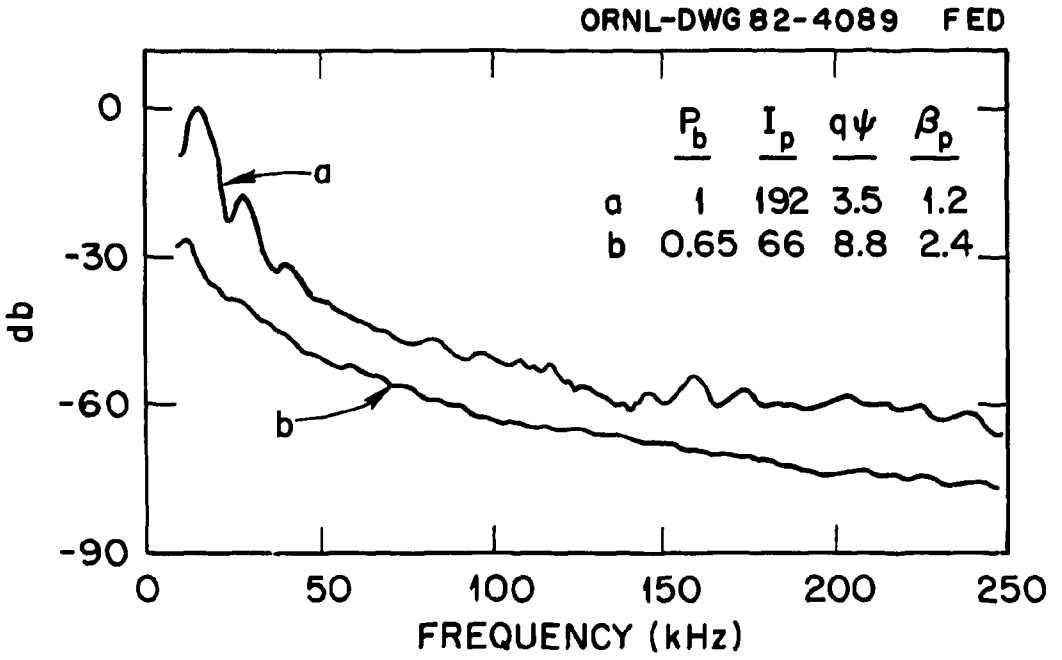

Fig. 3. $\tilde{B}_p$ power spectra measured 4 cm behind the limiter near the equatorial plane on the outside for a discharge (a) with significant plasma volume within the q = 1 surface and (b) with no detectable q = 1 surface in the plasma.

ORNL-PHOTO 0002-83 FED

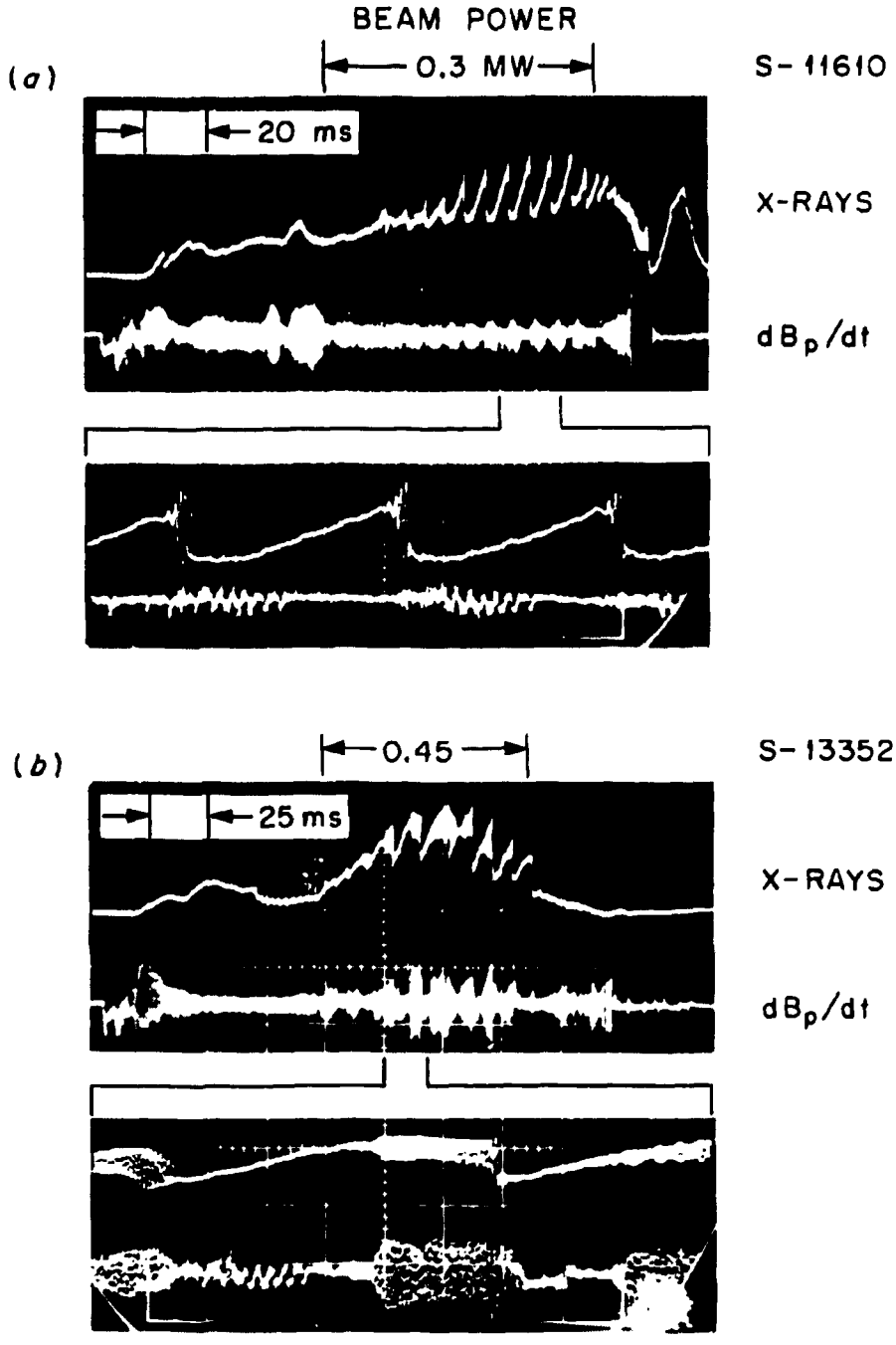

Fig. 4. X-ray and Mirnov coil signals. Fluctuations in the latter after the internal disruptions are a response to feedback-controlled power supplies, not to MHD activity.

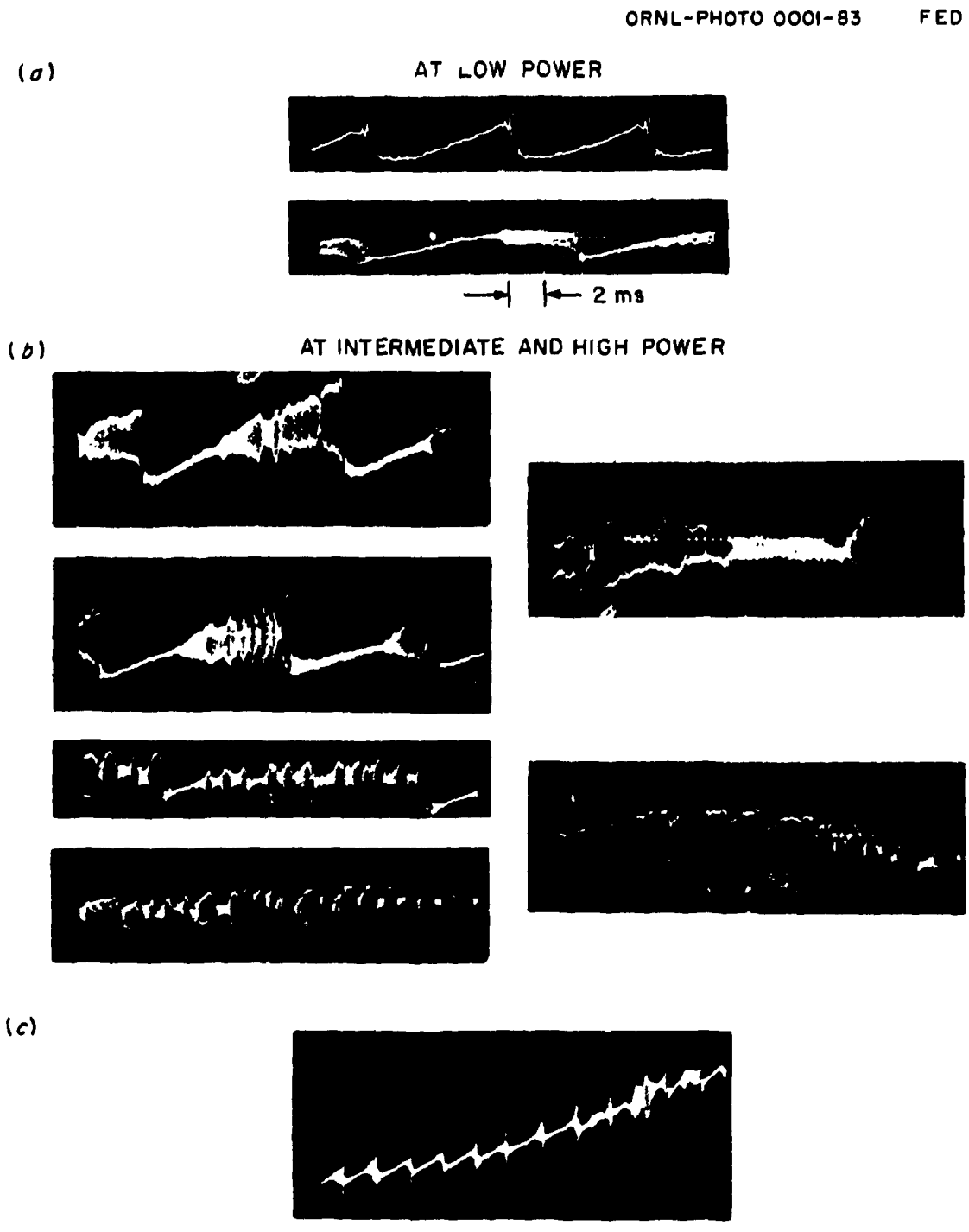

Fig. 5. X traces indicating the variety of signal patterns displayed by the experiment.

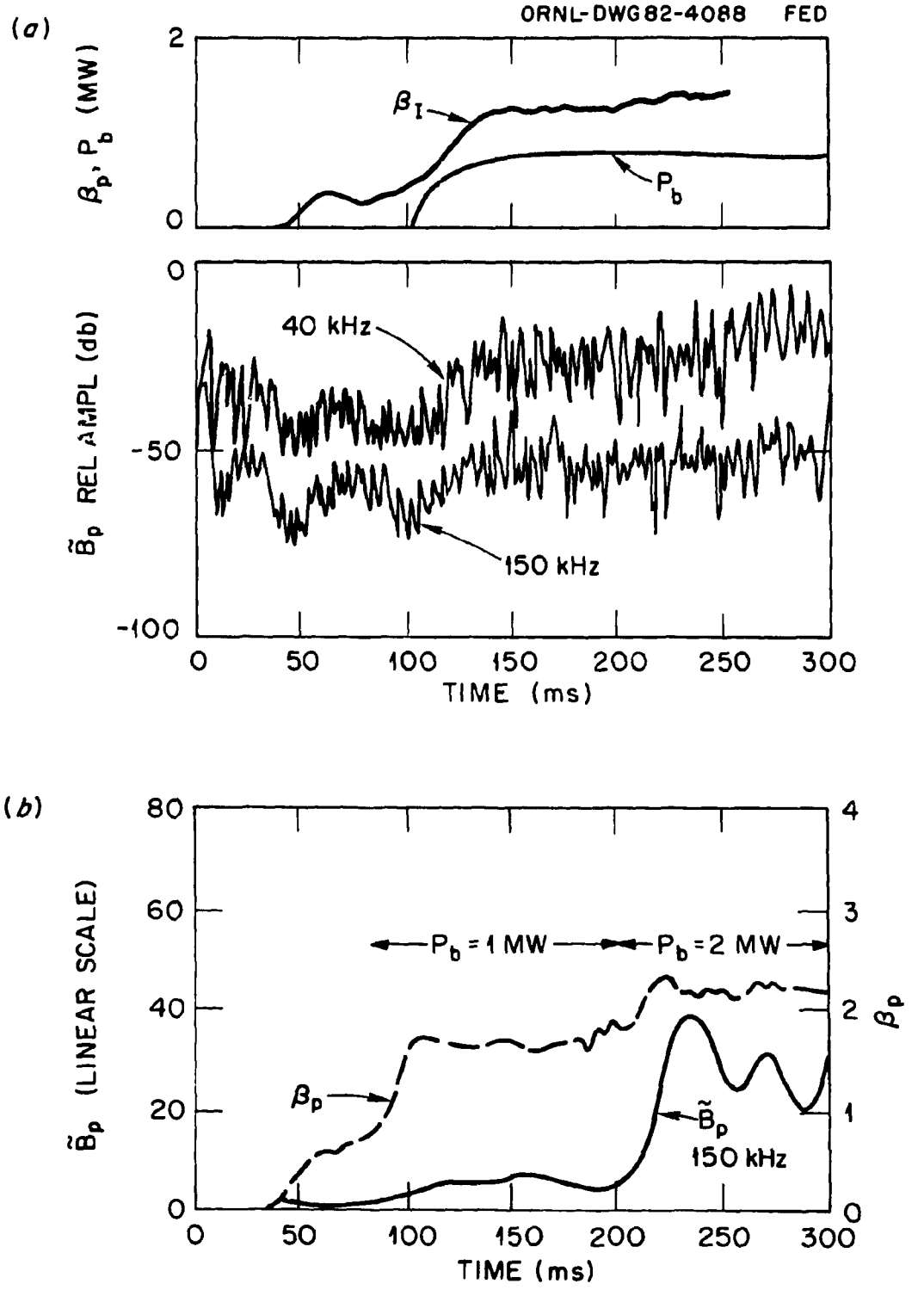

Fig. 6. $\tilde{B}_p$ and β_p changes with neutral beam injection.

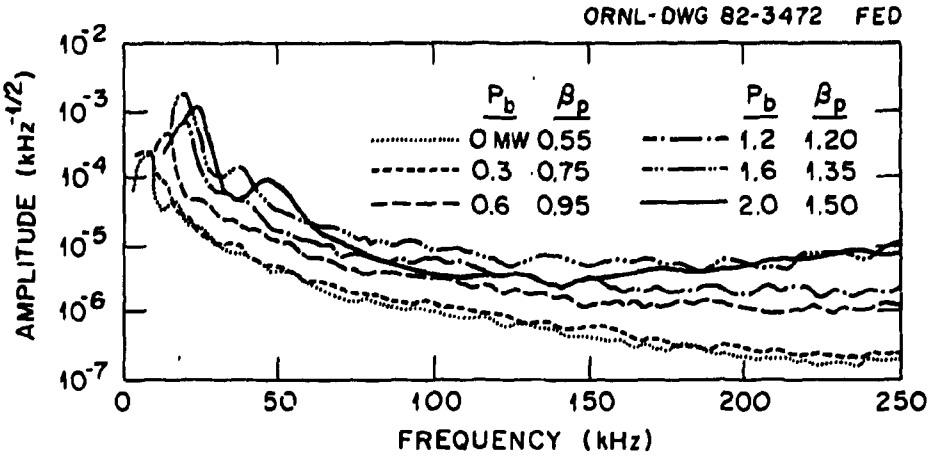

Fig. 7. Amplitude spectra of $\tilde{B}_p/B_p$ for the ISX-B P_b scan. Held constant were $B_T \approx 1.25$ T, $I_p \approx 185$ kA, and $\bar{n}_e(0) \approx 4 \times 10^{13}$ cm^{-3}.

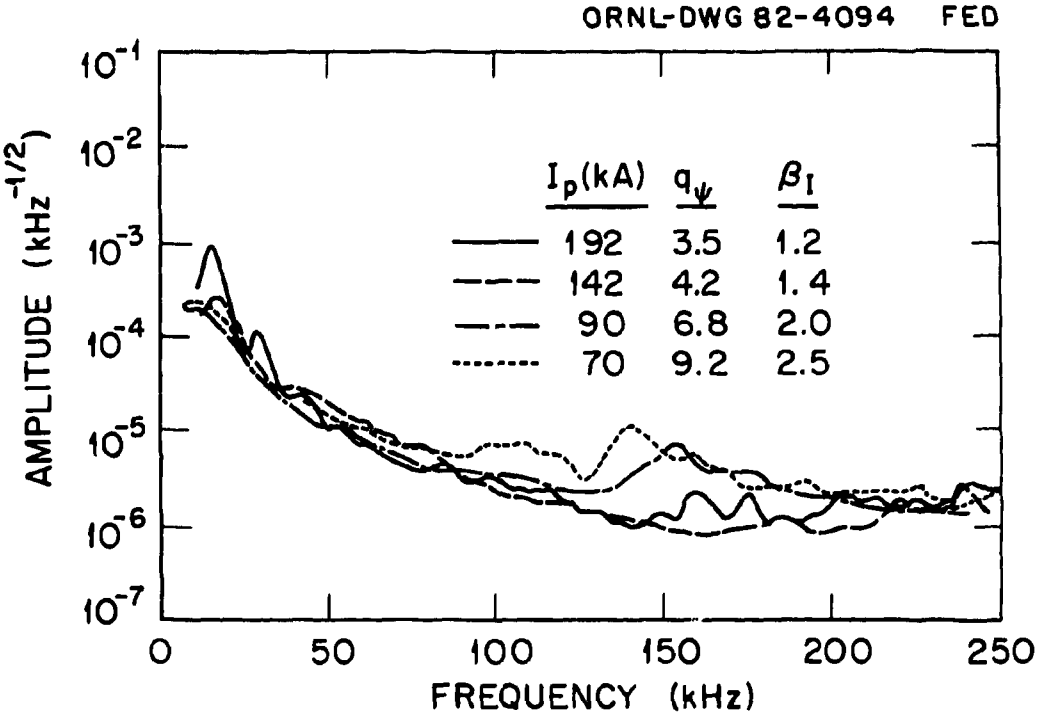

Fig. 8. Amplitude spectra of $\tilde{B}_p/B_p$ for the ISX-B I_p scan. Held constant were B_T = 1.3 T, P_b = 1 MW, and $\bar{n}_e(0)$ = 3.3 × 10^{13} cm^{-3}.

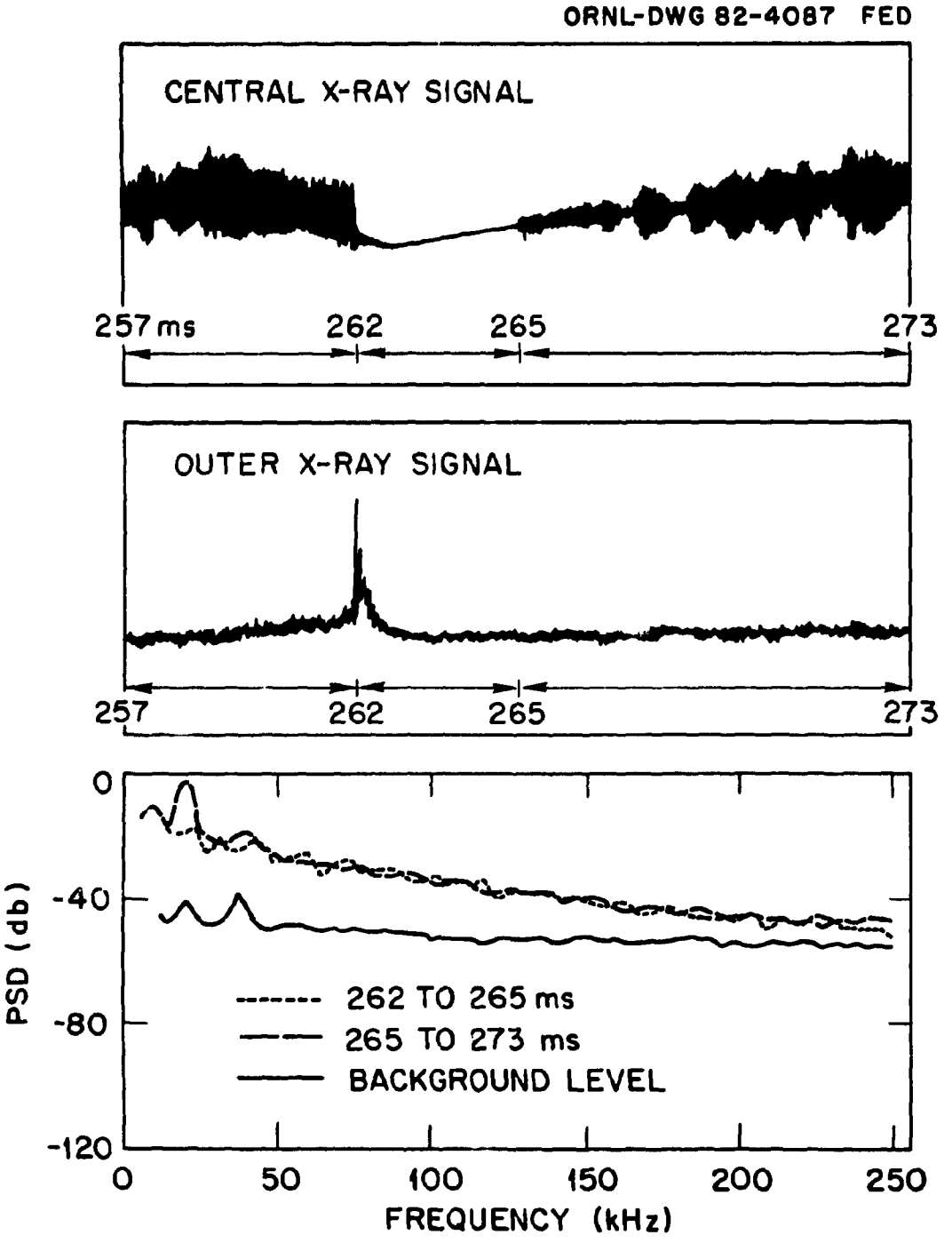

Fig. 9. Central and outer x-ray signals with power spectra for the latter during two time intervals. The central signal shows dominance by the (m = 1;n = 1) mode except in the interval following an internal disruption (262 to 265 ms).

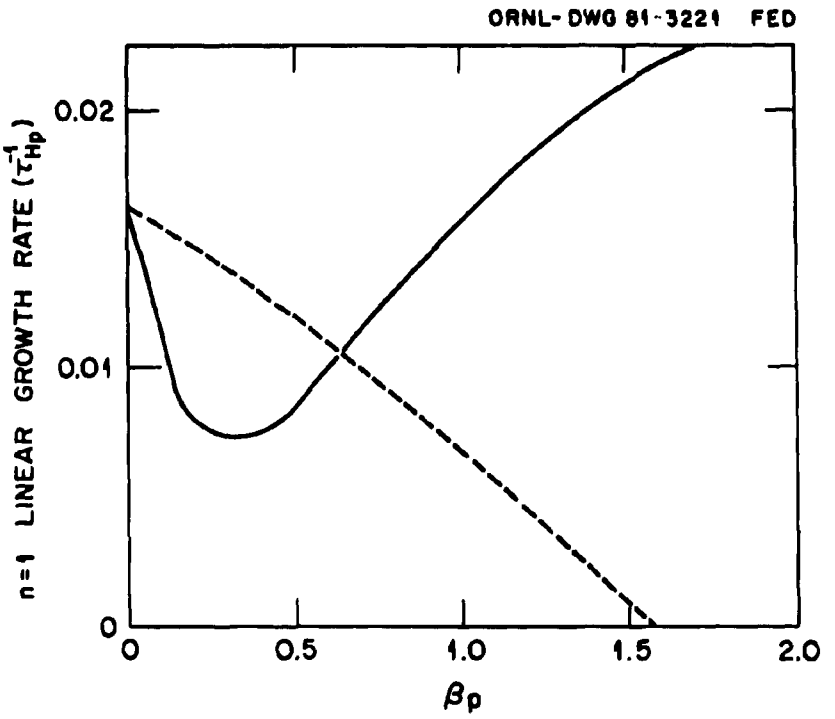

Fig. 10. n = 1 linear growth rate ($\sim \tau_{hp}^{-1}$) vs β_p for the flux-conserving sequence of equilibria described in the text. The dashed curve includes only the current-driven part of the mode, while the solid curve includes the full dynamic effects of the pressure-driving terms.

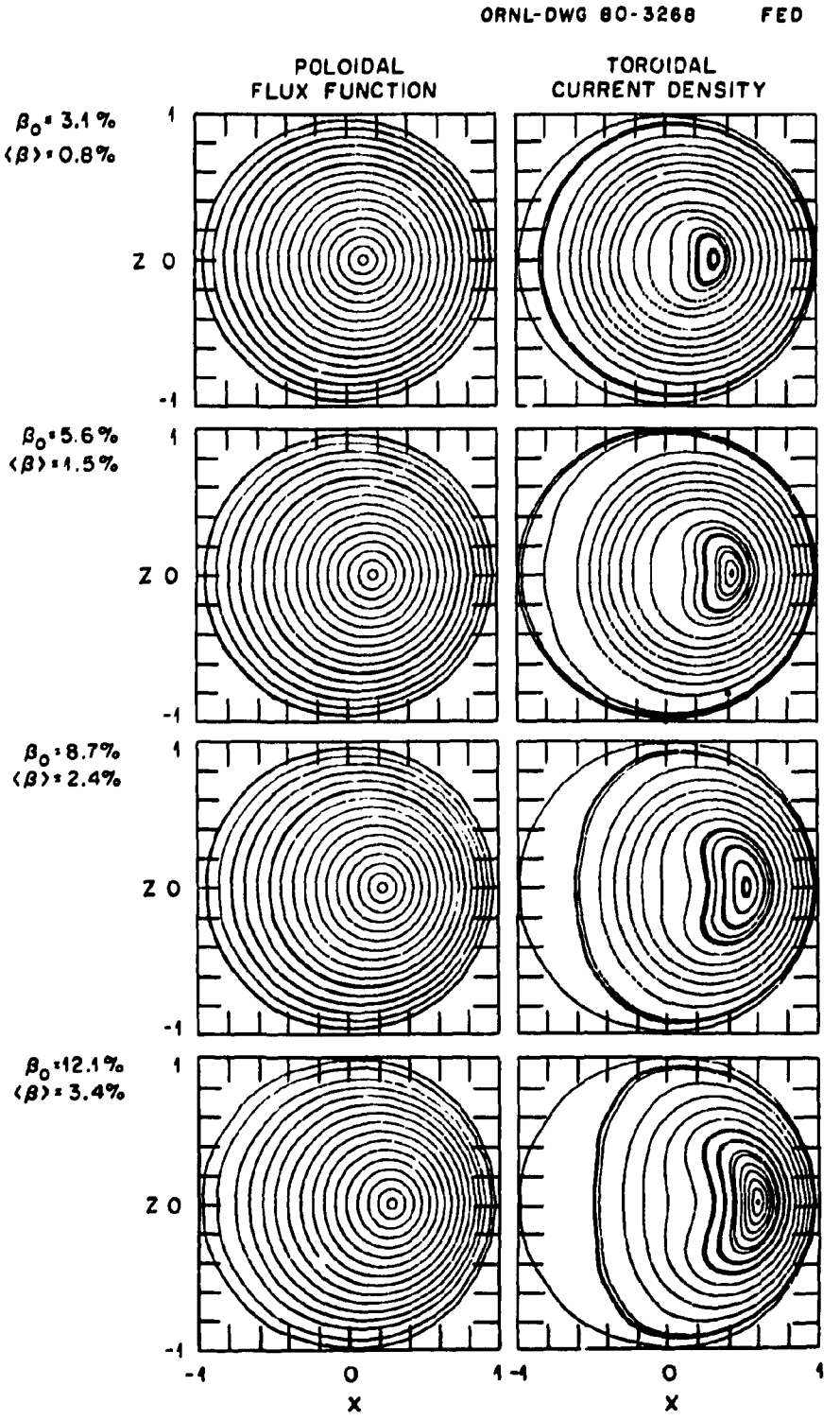

Fig. 11. Poloidal flux function Ψ and toroidal current density contours for the flux-conserving sequence of equilibria used to calculate the growth rates of Fig. 10.

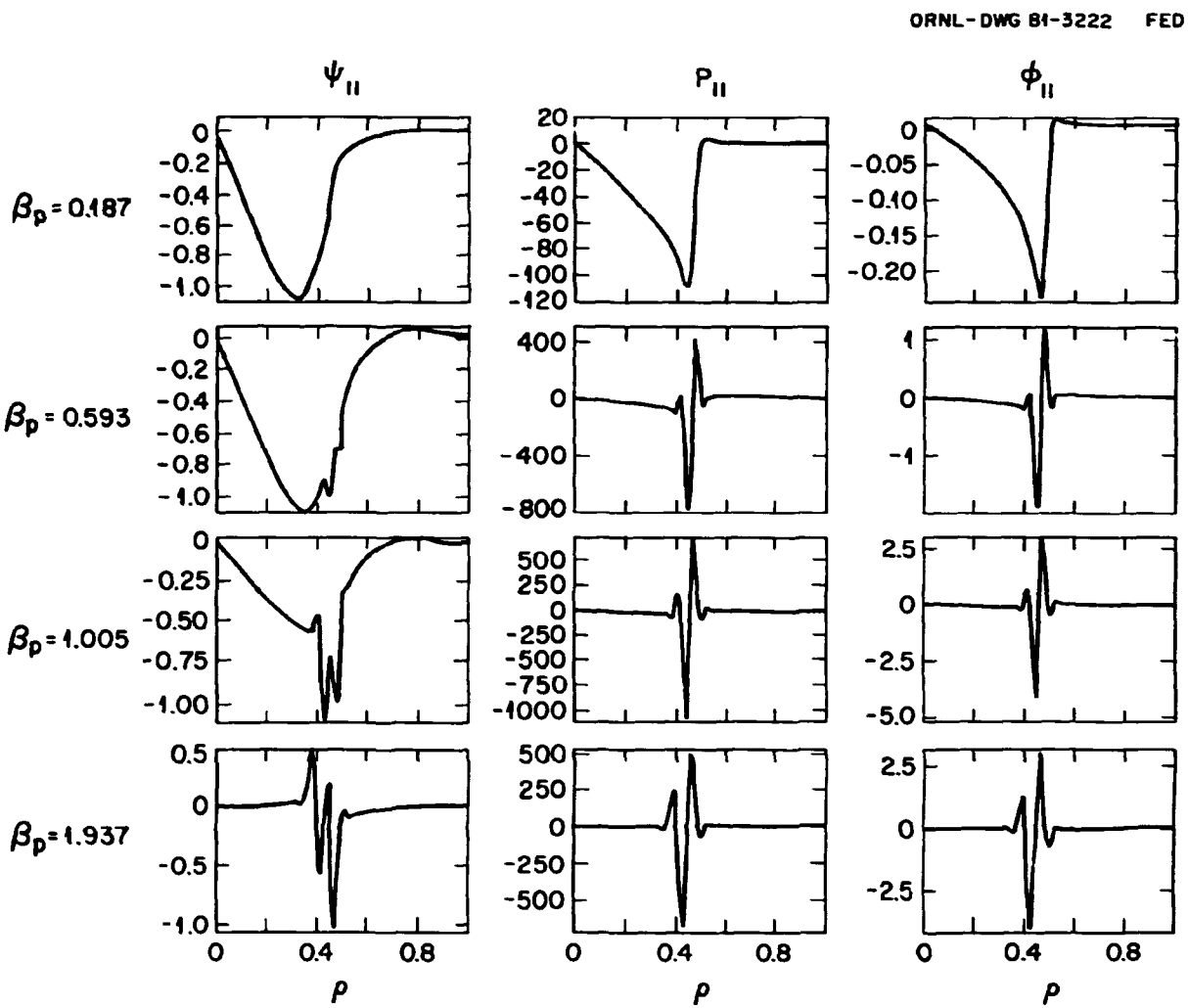

Fig. 12. m = 1 components of Ψ, P, and Φ for the n = 1 linear eigenmode for the β_p = 0.19, 0.59, 1.00, and 1.94 equilibria described in the text.

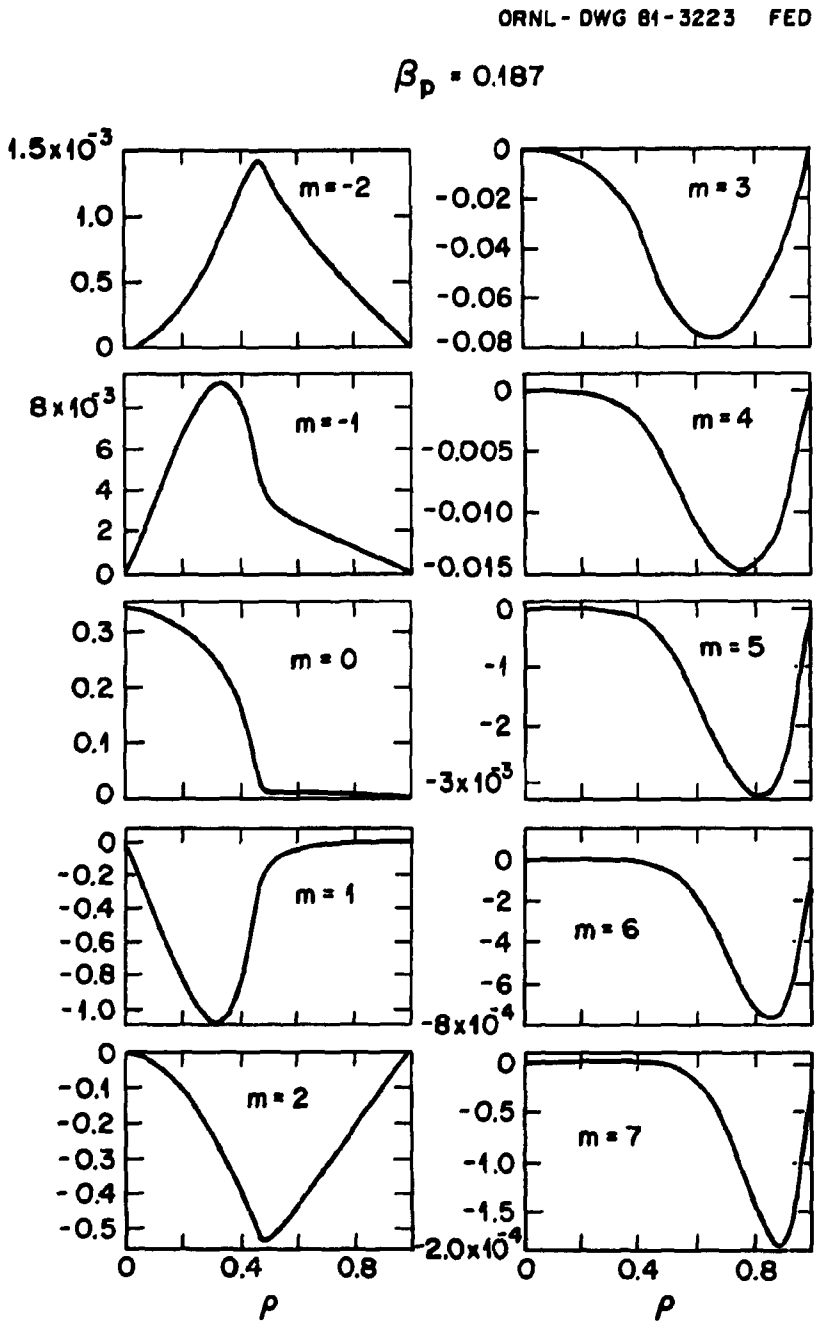

Fig. 13. m = -2, ..., 7 components of Ψ for the n = 1 eigenmode for the β_p = 0.19 equilibrium described in the text.

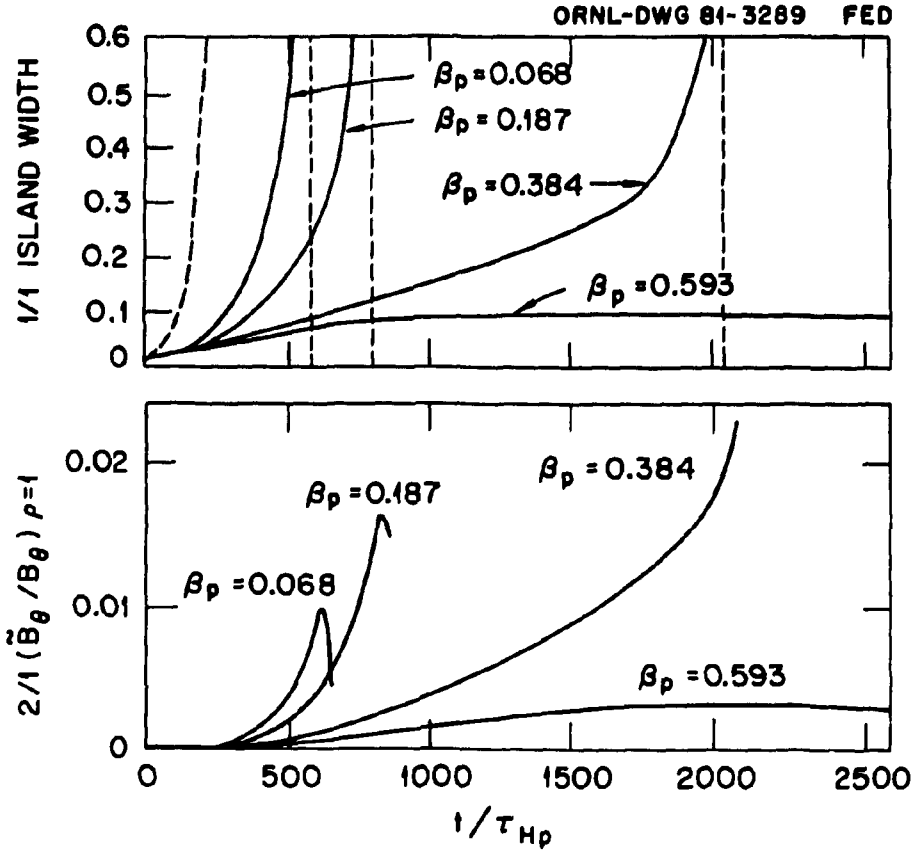

Fig. 14. m = 1/n = 1 magnetic island width (top) and (m = 2;n = 1) poloidal magnetic field fluctuation amplitude at the plasma edge (bottom) vs time for the β_p = 0.07, 0.19, 0.38, and 0.59 equilibria described in the text.

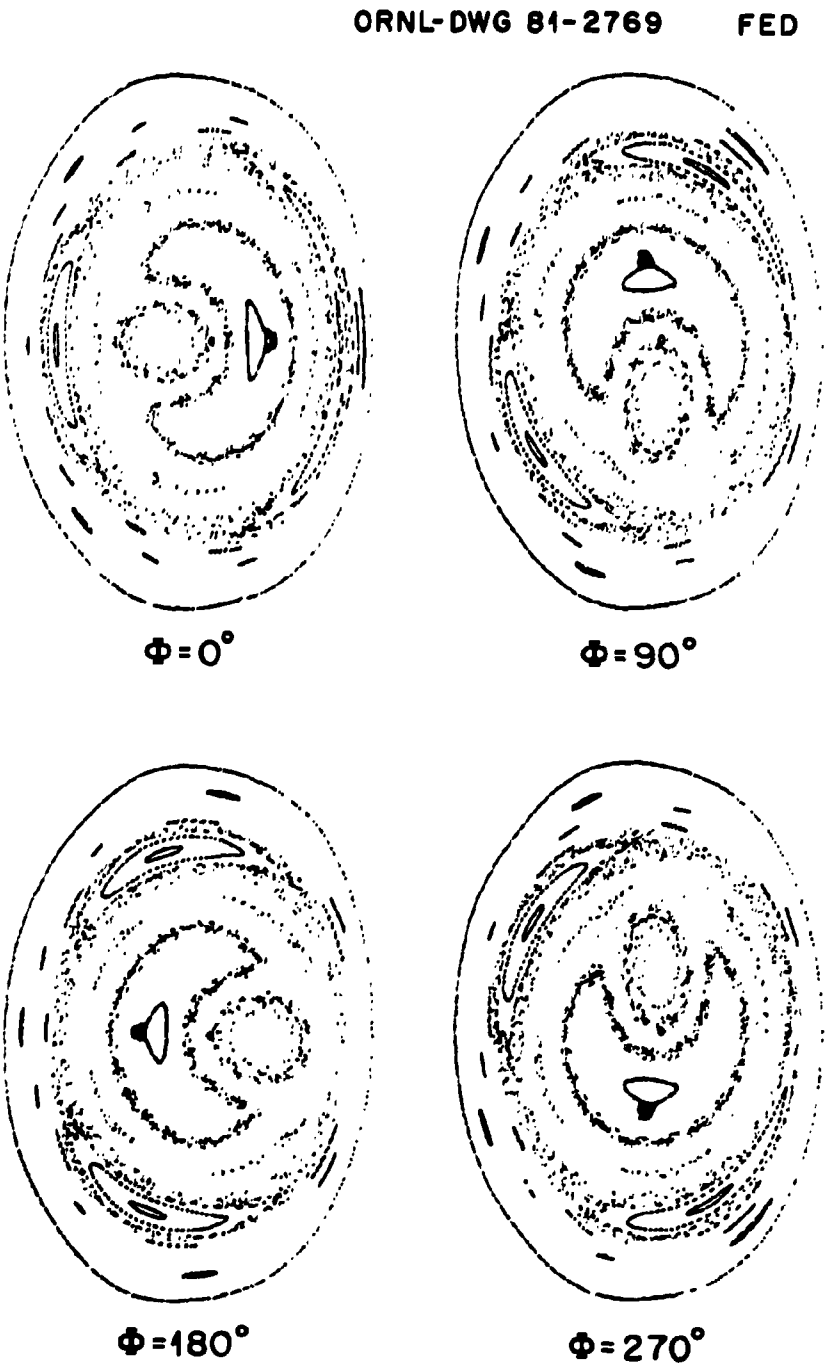

Fig. 15. Magnetic field line plot on four poloidal planes for an $n = 1$ driven instability.

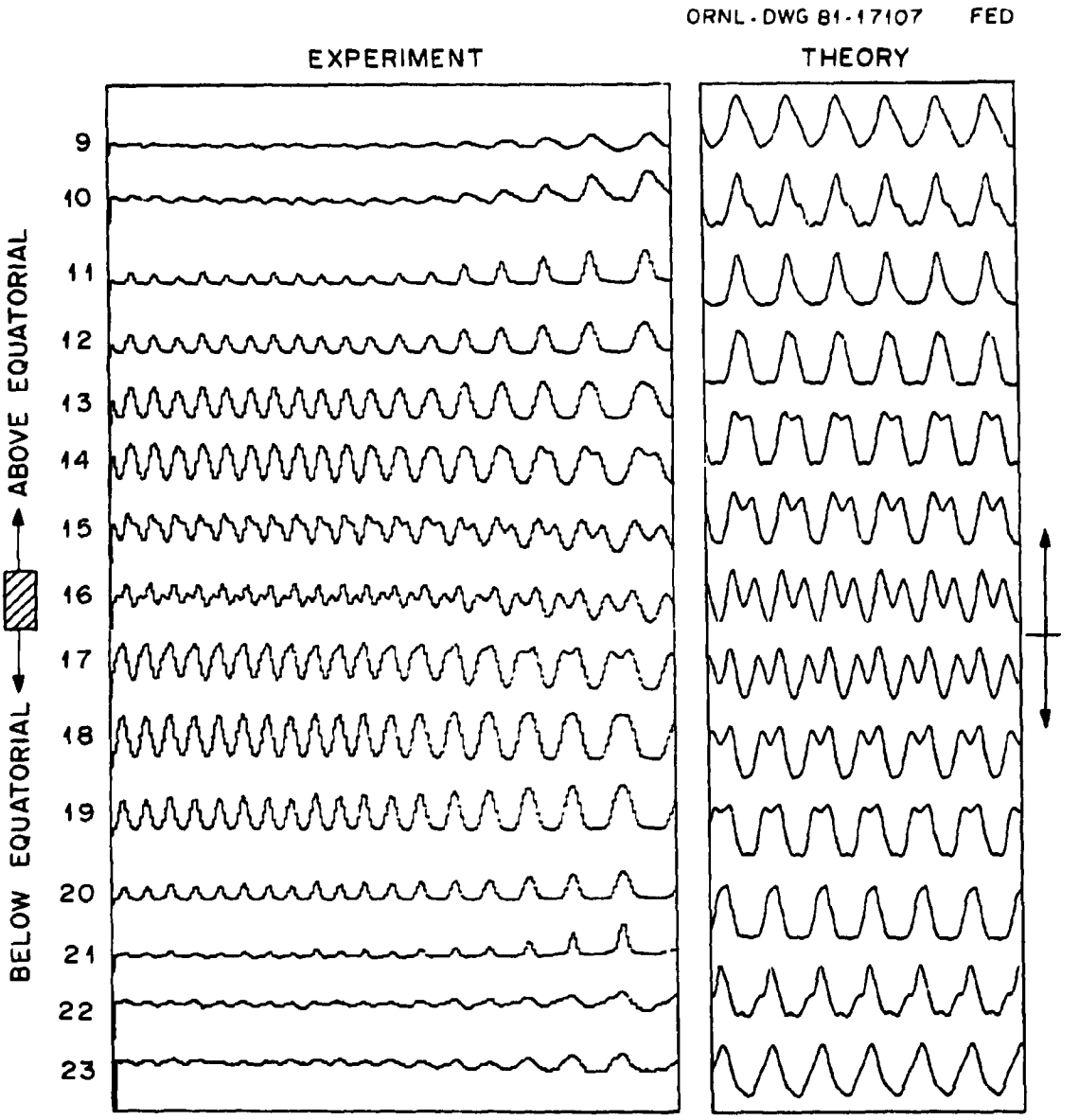

Fig. 16. Side-array waveforms, from 242 to 243.33 ms in the experiment. Viewing radii of the detectors, referenced to plasma center, step in equal increments from r = 0 to r = 0.15 m.

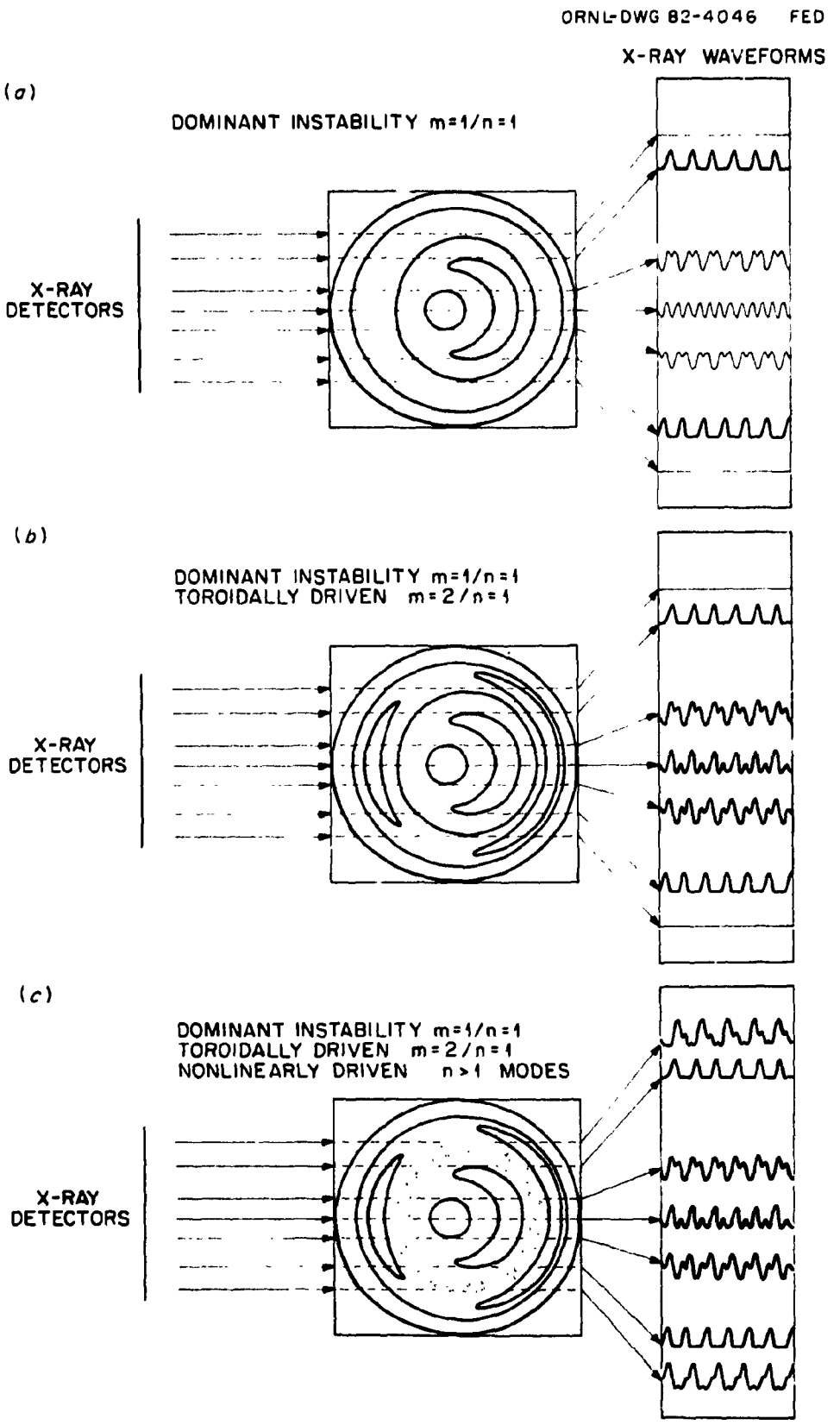

Fig. 17. Schematic representation of the origin of the X waveforms.

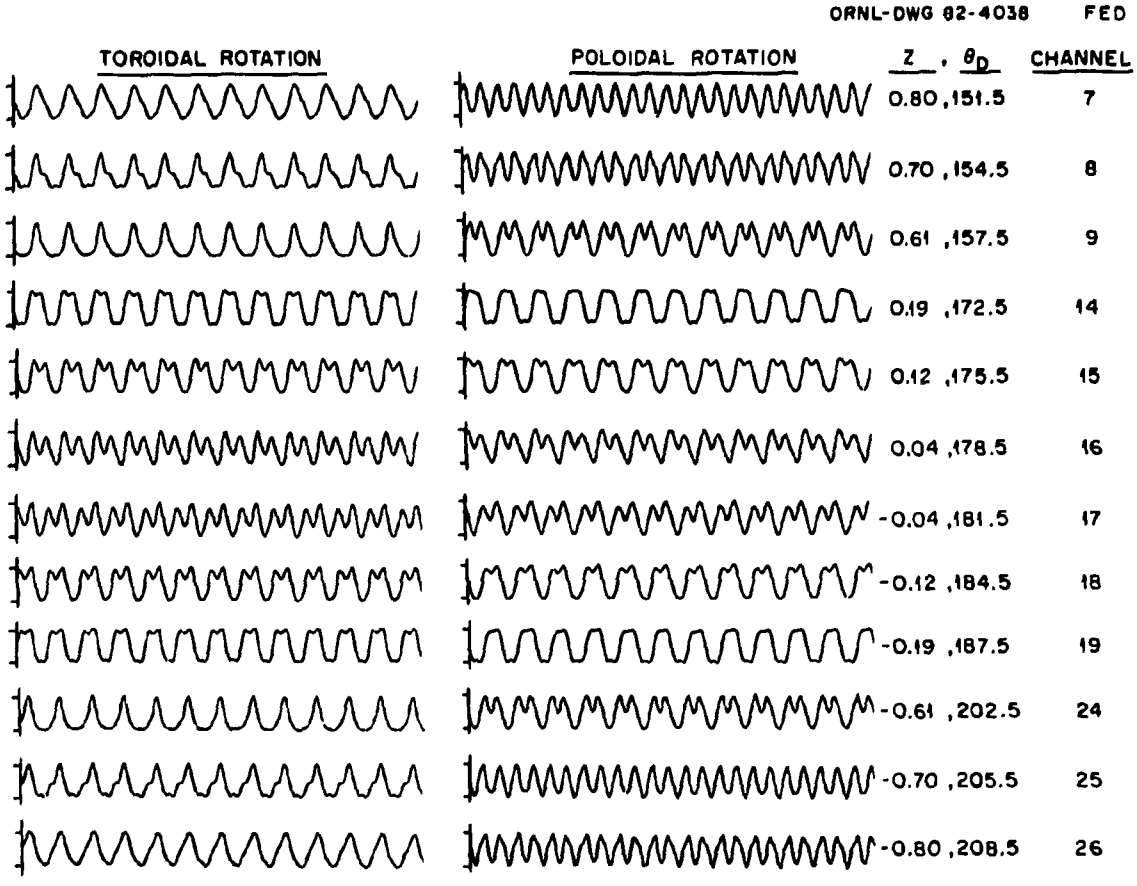

Fig. 18. Model waveforms for the side-mounted array resulting from toroidal or poloidal rotation of the instability structure shown in Fig. 15.

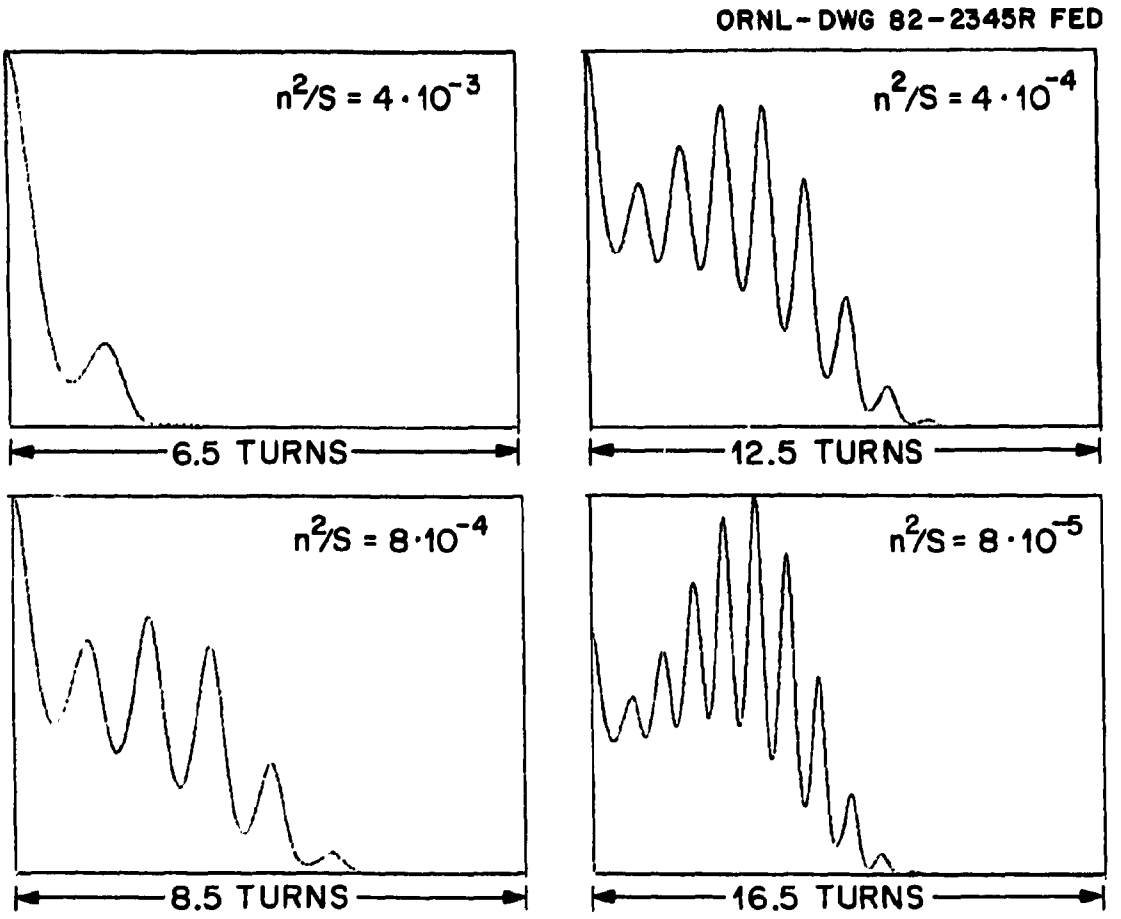

Fig. 19. Linear eigenfunctions of the resistive ballooning Eq. (8) for different values of the parameter n^2/S. The calculation was done for an analytic equilibrium described in the text with $\beta_p = 0.6$.

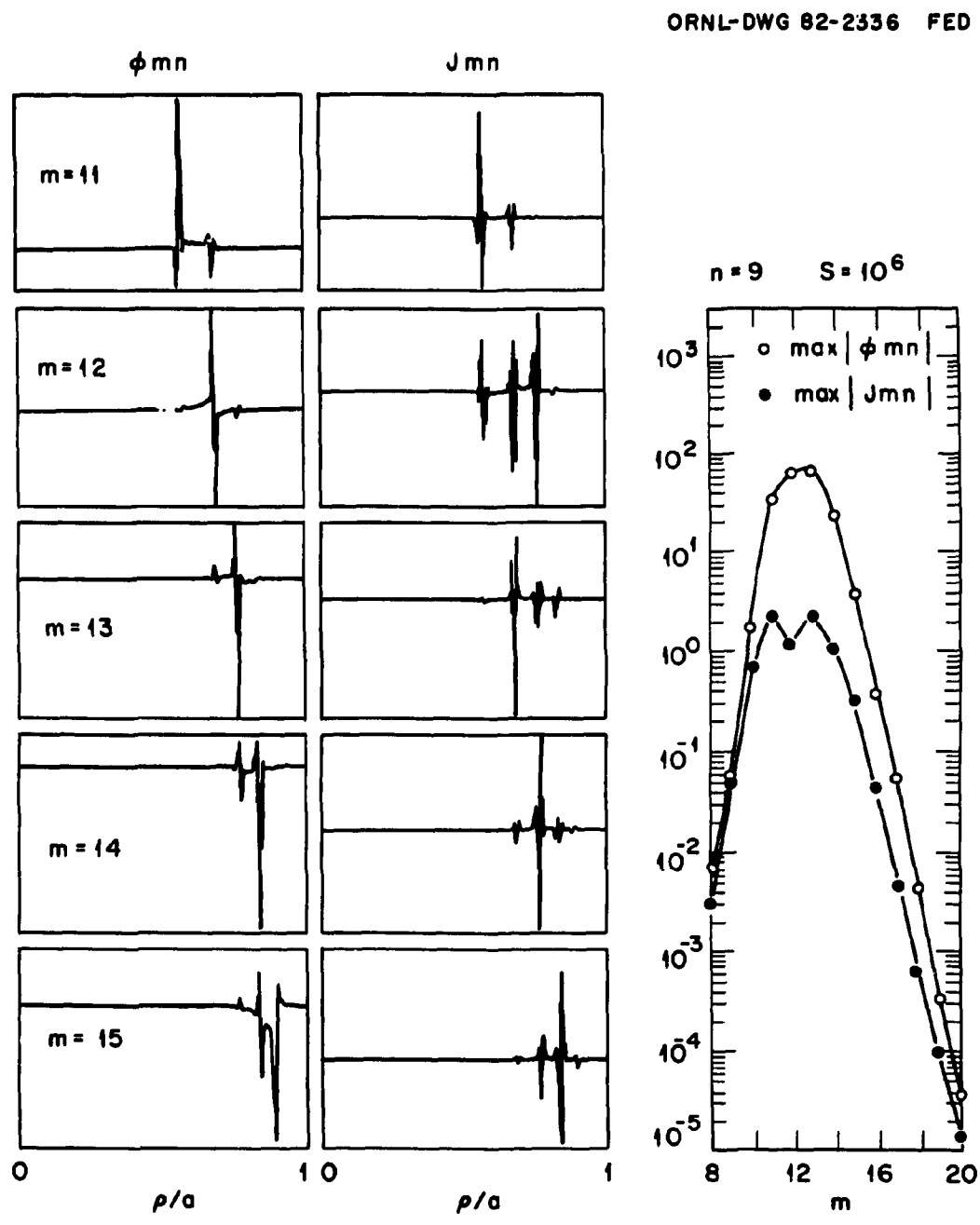

Fig. 20. Linear eigenfunction of the n = 9 mode for the same case as Fig. 19. The calculation was done here in real space using the RST code.

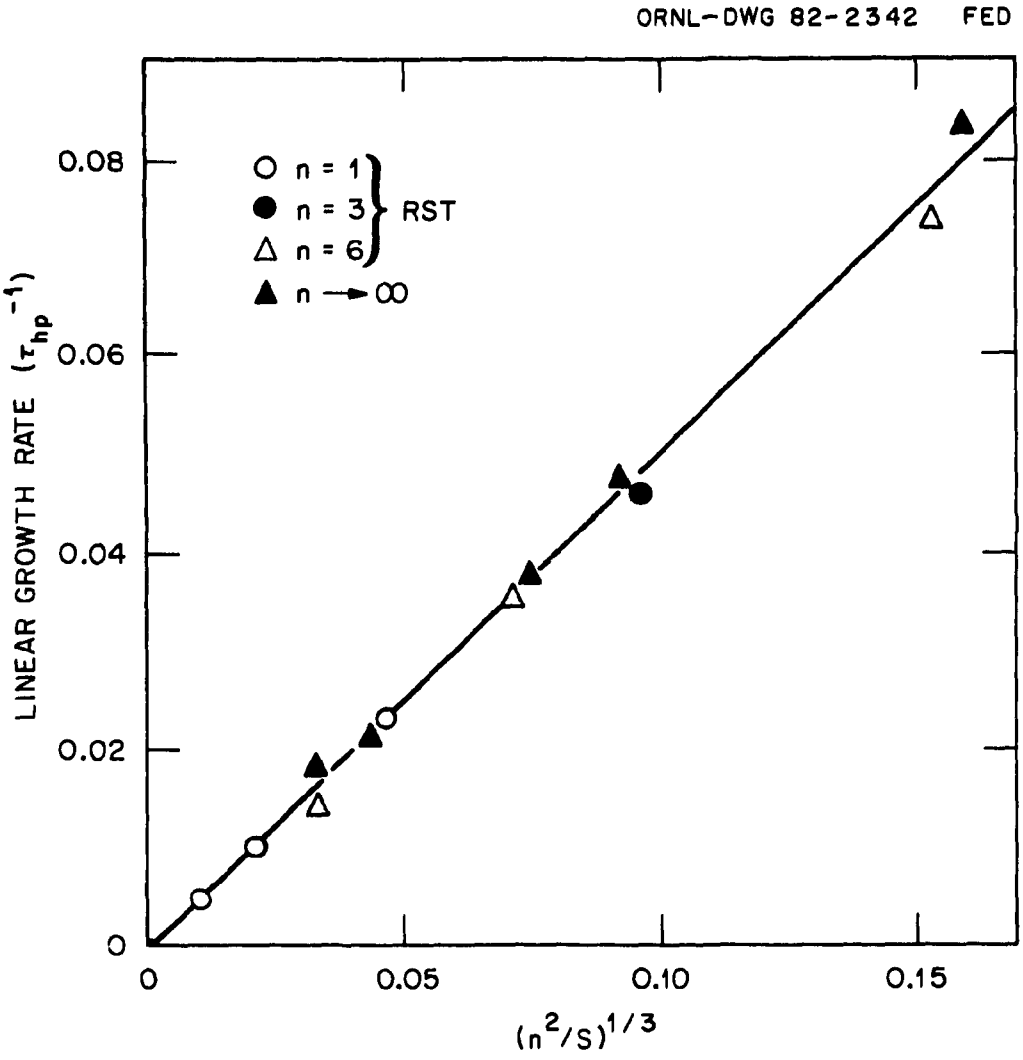

Fig. 21. Linear growth rate vs $(n^2/S)^{1/3}$ of the n = 1, n = 3, and n = 6 modes compared with the growth rate obtained using the resistive ballooning Eq. (8).

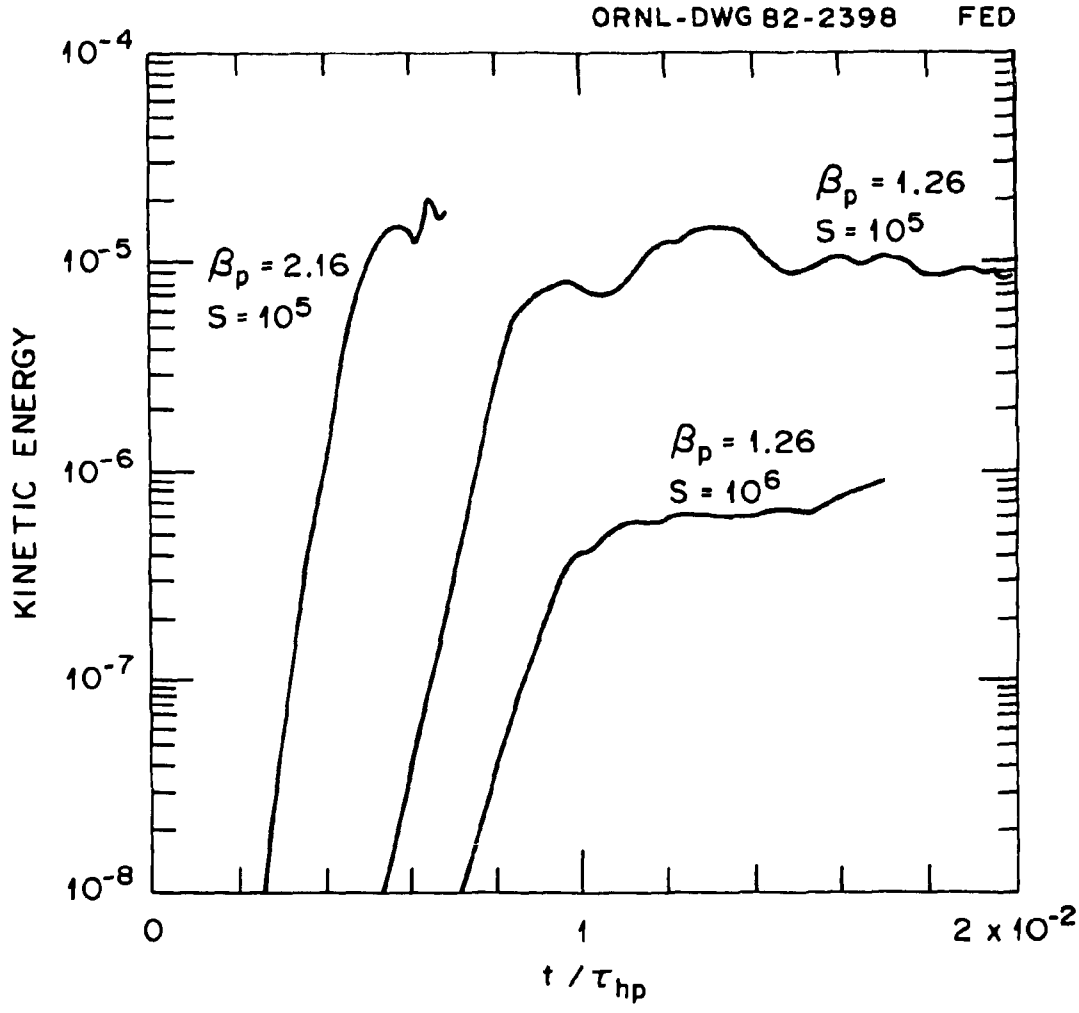

Fig. 22. Time evolution of the total kinetic energy from three many-mode (81 modes), nonlinear 3-D runs of RST code with equilibria described in the text and different values of S.

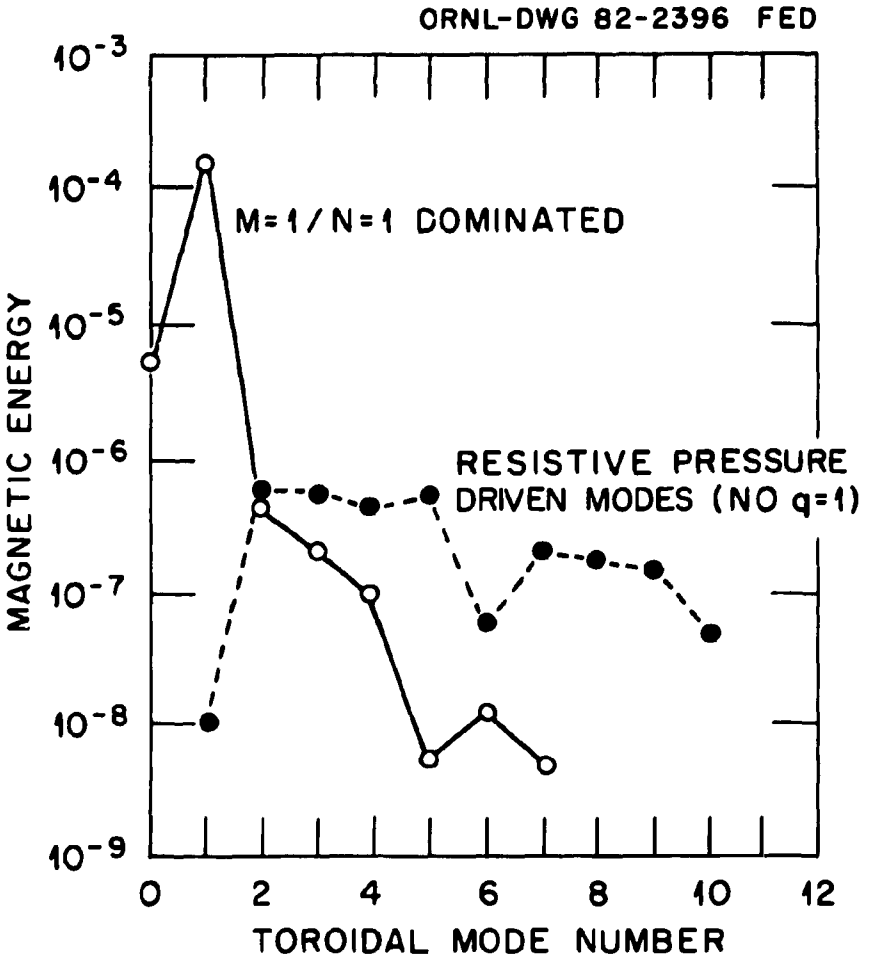

Fig. 23. Magnetic energy spectrum for a nonlinear 3-D many-mode run: (a) for an equilibrium of the flux-conserving sequence shown in Fig. 11 before magnetic field line reconnection, and (b) for the $S = 10^6$, $\beta_p = 1.26$ case shown in Fig. 22, where the $q = 1$ surface is not in the plasma.

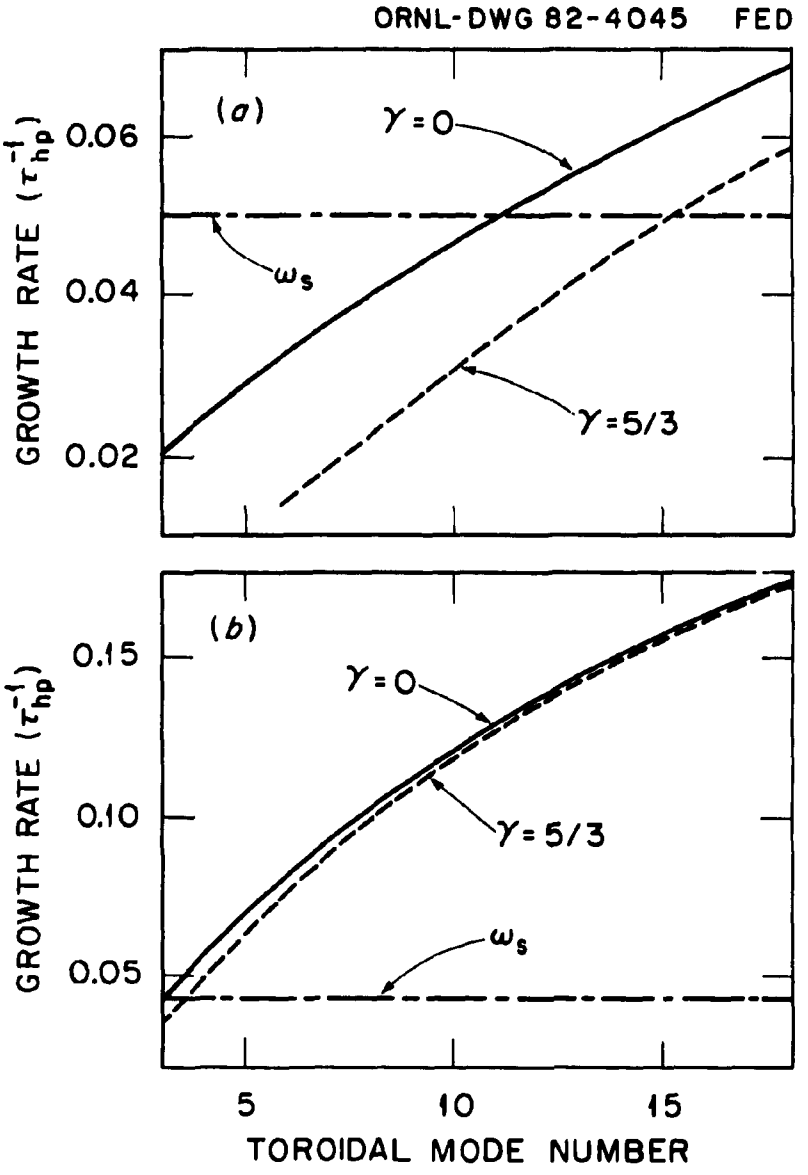

Fig. 24. Effects of parallel dynamics on growth rates in the ballooning limit. Linear growth rate vs n for (a) an equilibrium of the sequence described in the text with $\beta_p = 0.6$ and (b) an ISX-B equilibrium with $\beta_p = 1.6$, $q(0) = 0.9$, and $q_\psi = 4.3$. Here, γ is the ratio of specific heats and $\eta_{eq}(\rho)/S = 10^{-5}$.

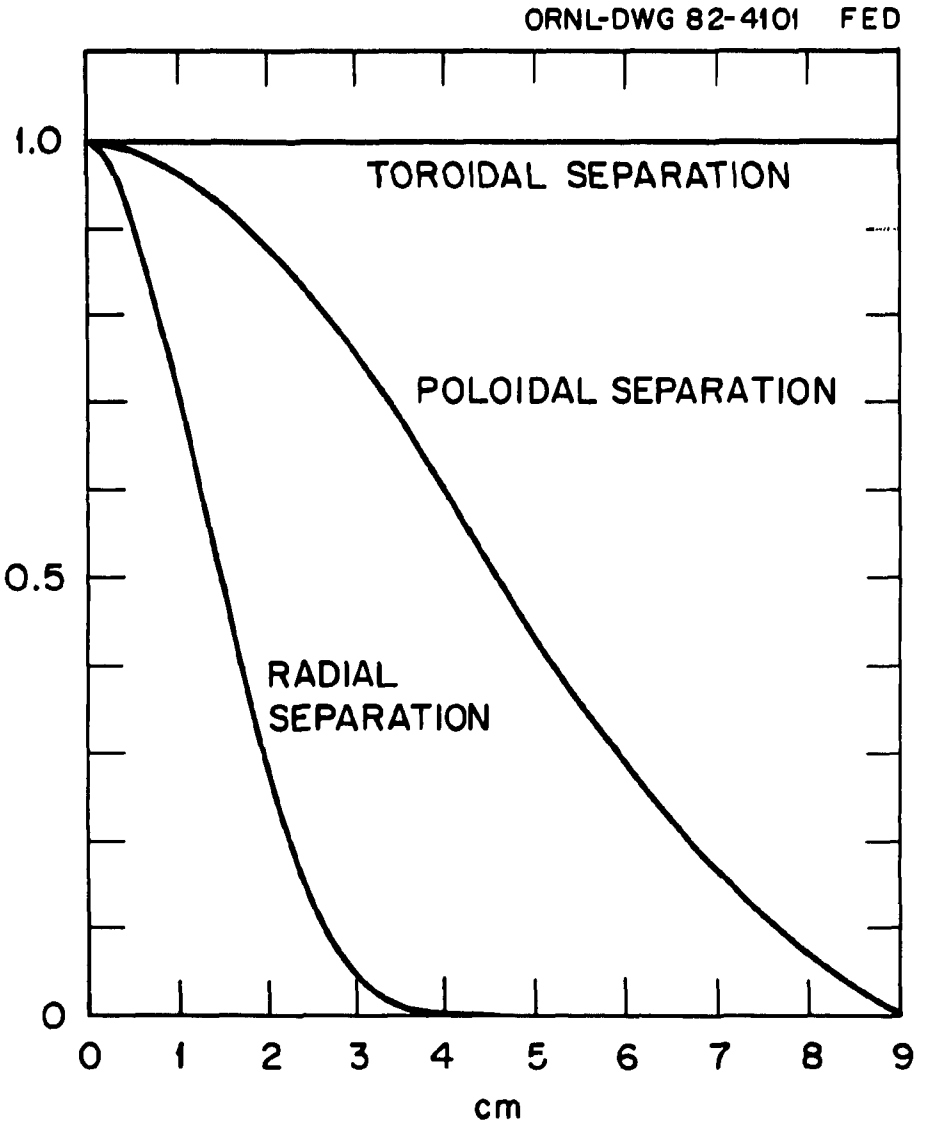

Fig. 25. Poloidal magnetic field autocorrelation functions of toroidal, poloidal, and radial separation, for the $\beta_p = 1.26$, $S = 10^6$ case shown in Fig. 22.

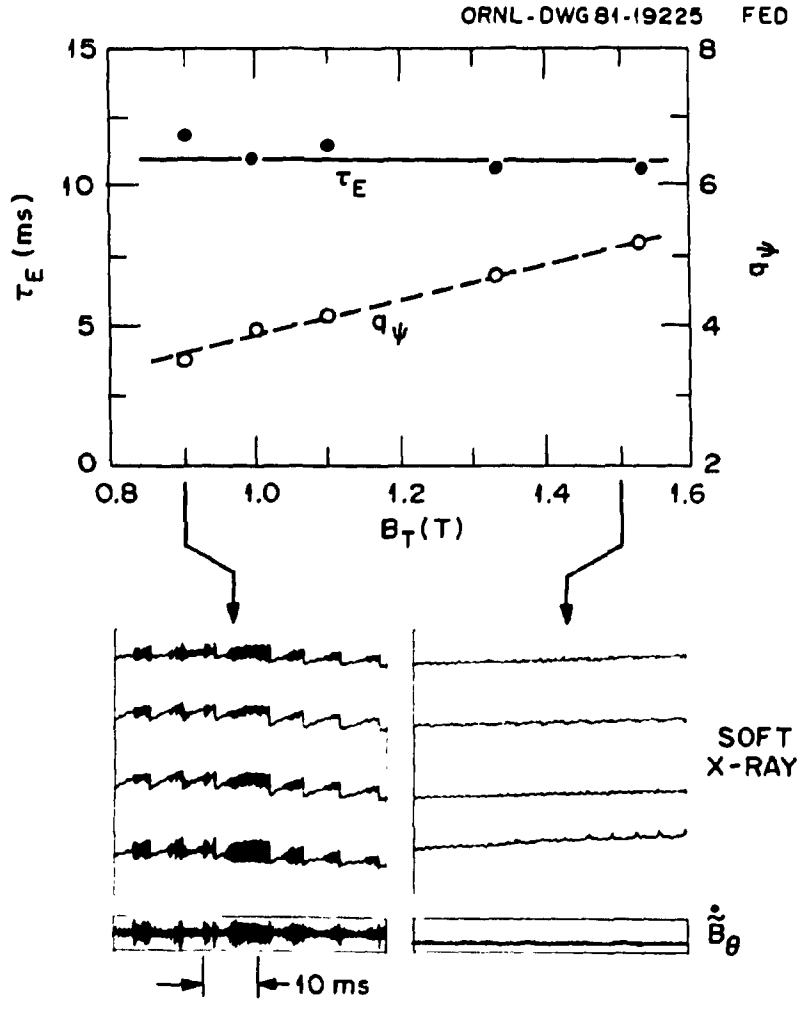

Fig. 26. Plasma parameters and representative instability signals for the ISX-B B_T scan. Held fixed were P_b = 0.6 MW, I_p = 140 kA, and $\bar{n}_e(0) \approx 6.5 \times 10^{13}$ cm^{-3}.

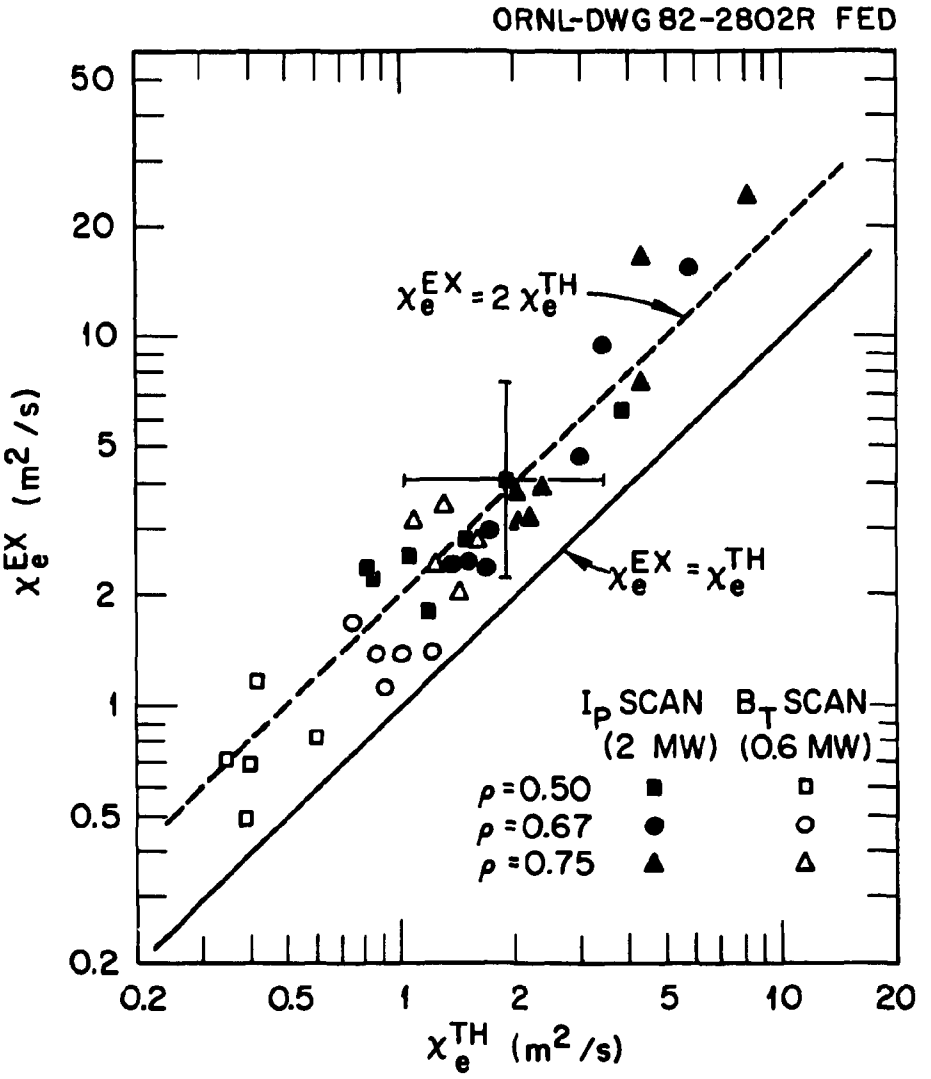

Fig. 27. Comparison of values of χ_e^{TH} and χ_e^{EX}.

ORNL/TM-8648
Dist. Category UC-20

INTERNAL DISTRIBUTION

1. J. D. Bell
2-6. B. A. Carreras
7. L. A. Charlton
8. W. A. Cooper
9. P. H. Diamond
10. R. A. Dory
11-15. J. L. Dunlap
16. T. C. Hender
17. H. R. Hicks
18. J. A. Holmes
19. V. E. Lynch
20. M. Murakami
21. V. K. Pare
22. Y-K. M. Peng
23. J. Sheffield
24. D. J. Sigmar
25. P. L. Similon
26. R. M. Wieland
27. A. J. Wootton
28. Laboratory Records, ORNL-RC
29. Document Reference Section
30-31. Laboratory Records Department
32. Central Research Library
33. Fusion Energy Division Library
34. Fusion Energy Division Reports Office
35. ORNL Patent Office

EXTERNAL DISTRIBUTION

36. Office of the Assistant Manager for Energy Research and Development, Department of Energy, Oak Ridge Operations, P.O. Box E, Oak Ridge, TN 37830
37. J. D. Callen, Department of Nuclear Engineering, University of Wisconsin, Madison, WI 53706
38. R. W. Conn, Department of Chemical, Nuclear, and Thermal Engineering, University of California, Los Angeles, CA 90024
39. S. O. Dean, Director, Fusion Energy Development, Science Applications, Inc., 2 Professional Drive, Gaithersburg, MD 20760
40. H. K. Forsen, Bechtel Group, Inc., Research Engineering, P.O. Box 3965, San Francisco, CA 94105
41. R. W. Gould, Department of Applied Physics, California Institute of Technology, Pasadena, CA 91125
42. D. G. McAlees, Exxon Nuclear Company, Inc., 777 106th Avenue, NE, Bellevue, WA 98009
43. P. J. Reardon, Princeton Plasma Physics Laboratory, P.O. Box 451, Princeton, NJ 08540
44. W. M. Stacey, Jr., School of Nuclear Engineering, Georgia Institute of Technology, Atlanta, GA 30332
45. G. A. Eliseev, I. V. Kurchatov Institute of Atomic Energy, P.O. Box 3402, 123182 Moscow, U.S.S.R.
46. V. A. Glukhikh, Scientific-Research Institute of Electro-Physical Apparatus, 188631 Leningrad, U.S.S.R.
47. I. Spighel, Lebedev Physical Institute, Leninsky Prospect 53, 117924 Moscow, U.S.S.R.
48. D. D. Ryutov, Institute of Nuclear Physics, Siberian Branch of the Academy of Sciences of the U.S.S.R., Sovetskaya St. 5, 630090 Novosibirsk, U.S.S.R.

49. V. T. Tolok, Kharkov Physical-Technical Institute, Academical St. 1, 310108 Kharkov, U.S.S.R.
50. R. Varma, Physical Research Laboratory, Navangpura, Ahmedabad, India
51. Bibliothek, Max-Planck Institut fur Plasmaphysik, D-8046 Garching bei Munchen, Federal Republic of Germany
52. Bibliothek, Institut fur Plasmaphysik, KFA, Postfach 1913, D-5170 Julich, Federal Republic of Germany
53. Bibliotheque, Centre de Recherches en Physique des Plasmas, 21 Avenue des Bains, 1007 Lausanne, Switzerland
54. Bibliotheque, Service du Confinement des Plasmas, CEA, B.P. 6, 92 Fontenay-aux-Roses (Seine), France
55. Documentation S.I.G.N., Departement de la Physique du Plasma et de la Fusion Controlee, Centre d'Etudes Nucleaires, B.P. No. 85, Centre du Tri, 38041 Cedex, Grenoble, France
56. Library, Culham Laboratory, UKAEA, Abingdon, Oxon, OX14 3DB, England
57. Library, FOM Institut voor Plasma-Fysica, Rijnhuizen, Jutphaas, The Netherlands
58. Library, Institute of Physics, Academia Sinica, Beijing, Peoples Republic of China
59. Library, Institute of Plasma Physics, Nagoya University, Nagoya 64, Japan
60. Library, International Centre for Theoretical Physics, Trieste, Italy
61. Library, Laboratorio Gas Ionizzati, Frascati, Italy
62. Library, Plasma Physics Laboratory, Kyoto University, Gokasho Uji, Kyoto, Japan
63. Plasma Research Laboratory, Australian National University, P.O. Box 4, Canberra, A.C.T. 2000, Australia
64. Thermonuclear Library, Japan Atomic Energy Research Institute, Tokai, Naka, Ibaraki, Japan

65-172. Given distribution as shown in TID-4500 Magnetic Fusion Energy (Category Distribution UC-20)

TABLE I

P_b (MW)	I_p (kA)	β_p	T_e (ρ=0.67) (eV)	W_n ($n^{-2/3}$)	γ_n ($10^4 n^{2/3} \cdot s^{-1}$)	ω_{*e} ($10^3 n \cdot s^{-1}$)	ω_S ($10^4 s^{-1}$)
2.0	83	1.70	86	14	5.0	5.7	2.7
2.0	192	1.05	253	44	2.7	7	9.1
1.0	184	1.05	309	55	2.0	10	9.9
0.6	143	0.85	103	38	4.3	6	3.3